Journal of South American Earth Sciences 92 (2019) 374–399

Contents lists available at ScienceDirect

Journal of South American Earth Sciences

journal homepage: www.elsevier.com/locate/jsames

# Magmatic evolution of the Cerro Maricunga gold porphyry-epithermal system, Maricunga belt, N-Chile

Stephanie Lohmeier[a,*,1], Albrecht Schneider[b], Boris Belyatsky[c], Bernd Lehmann[a]

[a] Mineral Resources, Technical University of Clausthal, Adolph-Roemer Str. 2A, 38678, Clausthal-Zellerfeld, Germany
[b] Atacama Pacific Gold Corporation, Avenida Presidente Kennedy 5757, Las Condes, Santiago, Región Metropolitana, Chile
[c] Karpinskii All-Russian Geological Institute of Geology (VSEGEI), Saint-Petersburg, 190121, Russia

ARTICLE INFO

*Keywords:*
Cerro Maricunga
Maricunga belt
Flat slab
Diatreme system
Gold mineralization

ABSTRACT

The Cerro Maricunga gold project is located in the Maricunga gold belt in northern Chile, within the remnant edifice of the Tertiary Ojo de Maricunga volcano. The gold mineralization is hosted within a 23–15 Ma old complex system of interwoven porphyry intrusions, flows, dikes and diverse breccia types, all forming part of a large diatreme system. In particular, phreatomagmatic and phreatic processes contributed to the formation of the synmineral diatreme complex. The rocks are calc-alkaline (daci)andesites and very rare dacites of the medium-K series with a high-K tendency and a conspicuous "adakitic" signature. Rare-earth element patterns reflect formation during a period of distinctly thickened continental crust with retention of heavy rare-earth elements by a garnet-bearing residue at a depth of ≥45 km. U-Pb zircon ages show a wide spectrum from Proterozoic, over Permian and Triassic ages to Paleocene, Oligocene, early and mid-Miocene ages. The Phanerozoic zircon ages indicate the assimilation of country rocks, whereas the Proterozoic age reflects the presence of a lower crustal Neoproterozoic basement that is also suggested by $\varepsilon_{Nd}$ values of −3.9 to −3.1 for bulk rock, i.e. mantle depletion model ages around 1 Ga. The last magmatic activity at the Ojo de Maricunga volcano was at ~14.9 Ma. Stable isotope data on hydrothermal barite and supergene acanthite and gypsum ($\delta^{34}S_{acanthite}$: −0.6 to −0.4; $\delta^{34}S_{sulfate}$: 0.2 to 4.6; $\delta^{18}O_{sulfate}$: 9.2 to 13.8) indicate an igneous origin of sulfur and arid conditions during mineral formation. The emplacement of the diatreme complex took place during the adjustment of the Chilean flat slab setting in a time of increased crustal thickness. Although the rocks at Ojo de Maricunga show a pronounced adakite-like signature, they formed in a common MASH zone or a deep hot zone within the lower crust. Gold mineralization took place at ~17.9 Ma (Re-Os on molybdenite), syngenetic with diatreme formation and emplacement of hydrous magma. The thickening of continental crust was more advanced in the northern part of the Maricunga belt in the early to mid-Miocene than previously assumed, and then shifted south where several younger gold porphyries formed.

## 1. Introduction

The Maricunga gold (-silver) belt (short: Maricunga belt), in northern Chile is a metallogenic province (26°00′–28°00′S and 69°00–69°30′W; McKee et al., 1994) in the transitional zone between the modern nonvolcanic flat-slab region to the south and the modern normal subduction region to the north, i.e. the Central (Andean) Volcanic Zone (CVZ; Fig. 1). This province is known for its transitional porphyry-epithermal Au-(Ag) deposits (i.a. Vila and Sillitoe, 1991; Muntean and Einaudi, 2001), and has a quite diversified magmatic-volcanic history with five discrete Cenozoic magmatic-tectonic episodes (Mpodozis et al., 1995), that evolved concurrent with the thickening of the crust due to the decrease of the subduction angle over the last 30 Ma (i.a. Kay et al., 1999; Bissig et al., 2003). As a result, the geochemical signature of igneous rocks changed substantially during the Cenozoic evolution, concomitant to the diminishing volcanic activity (i.a. Kay et al., 1987, 1988, 1991, 1999; Kay and Mpodozis, 2001, 2002). Mineralization in the Maricunga belt occurred in two major episodes during the progressive deepening of the stationary arc. The older event took place in late Oligocene to early Miocene (23–21 Ma; La Coipa; Oviedo et al., 1991; Sillitoe et al., 1991), the younger in mid-Miocene (13–10 Ma), including the emplacement of the so-called gold

* Corresponding author.
*E-mail addresses:* lohmeier@mre.rwth-aachen.de (S. Lohmeier), albrecht.schneider@sbx.cl (A. Schneider), bbelyatsky@hotmail.ru (B. Belyatsky), lehmann@min.tu-clausthal.de (B. Lehmann).
[1] Institute of Mineral Resources Engineering, RWTH Aachen University, Lochnerstraße 4–20, 52062, Aachen, Germany (present address).

https://doi.org/10.1016/j.jsames.2019.03.003
Received 9 June 2018; Received in revised form 5 March 2019; Accepted 5 March 2019
Available online 09 March 2019
0895-9811/ 

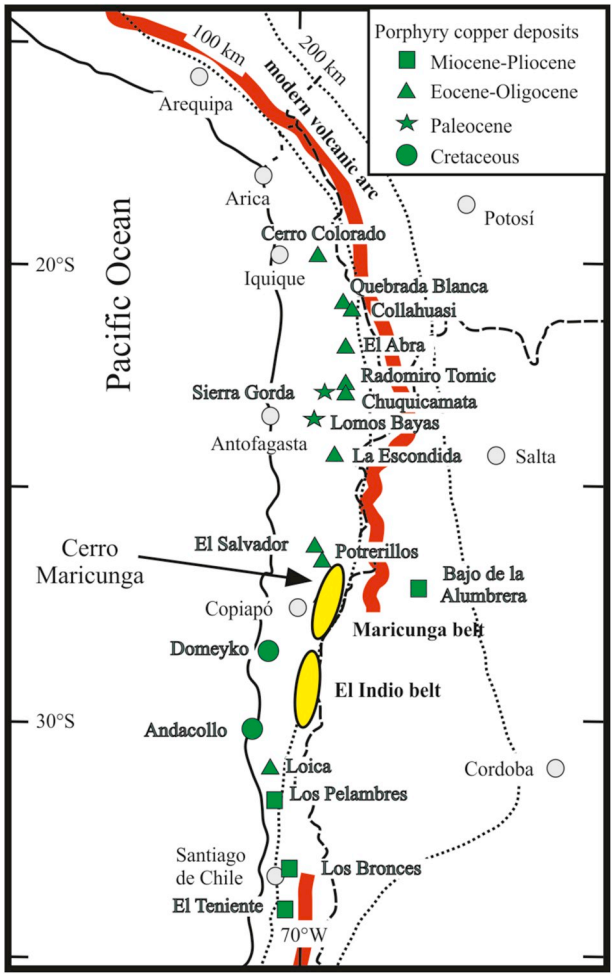


**Fig. 1.** Tectonic setting and location of the Maricunga belt between the northern boundary of the modern nonvolcanic flat slab region of the Chilean Andes (28°–33°S) and the southern end of the CVZ, as well as the location of the mayor Chilean porphyry-copper deposits (modified after Lohmeier et al., 2013). Dotted lines show depths of the Wadati-Benioff zone. Dashed lines are frontiers.

porphyries of e.g. Marte-Lobo (Vila et al., 1991), La Pepa and Maricunga Mine (Vila and Sillitoe, 1991, Fig. 2). In between, a virtual volcanic lull is described for the period of 20 to 17 Ma (Mpodozis et al., 1995). Magmatic activity ceased in the whole belt in late Miocene to Pliocene with the latest events in the surroundings of volcano Nevado de Jotabeche, whose special geochemical signature reflects a crustal thickness of > 60 km (Mpodozis et al., 1995).

Starting in early Oligocene, ore formation between 20° and 27°S took place under continuously drier climatic conditions (Alpers and Brimhall, 1988; Evenstar et al., 2005). This climatic change directly affected the early mineralization stage in the belt, in particular by retreating groundwater tables with concomitant supergene enrichment processes (Sillitoe and McKee, 1996). The second stage of ore formation coincided with the establishment of super-arid conditions, i.e. the formation of the Atacama Desert.

The Cerro Maricunga gold project, not to be confounded with the Maricunga (Mine) gold deposit (see Fig. 2), is within the extinct, partially eroded Ojo de Maricunga volcano. The area is divided into four zones (Lynx, Pollux, Phoenix and Crux zone; Fig. 3), containing 5.2 Moz Au at a grade of 0.38 g/t Au (Conca et al., 2014). Greenfield exploration started in 2008, systematic exploration was done between 2009 and 2013 by trench, surface, drillcore and cutting mapping as well as geophysical investigations by Atacama Pacific (Lohmeier et al., unpublished results, a). In early May 2018 an agreement was made between Atacama Pacific and Rio2 to merge both companies with the aim to complete a feasibility study and start project development under the new name “Fenix project".

The exploration work allowed some research on the magmatic evolution of the Cerro Maricunga area and the data obtained may contribute to the understanding of the regional geology. Zircon U-Pb data and bulk-rock Sm-Nd data give direct evidence of the assimilation of Precambrian basement rocks in the evolving magma system. The timing of gold mineralization at the Ojo de Maricunga volcano contradicts the classical view of two discrete gold stages in the belt, in support of a more continuous spectrum of ore formation, and the establishment of arid climatic conditions played a role during the formation of the deposit.

## 2. Regional geologic setting

The Maricunga belt belongs to the western part of the Cordillera Domeyko and straddles the transition zone between the modern nonvolcanic flat slab region of the Chilean Andes (28°–33°S) and the southern end of the CVZ (14°–28°S). The regional geological situation described in detail in Mpodozis et al. (1995), and the more general work by Davidson and Mpodozis (1991), Vila and Sillitoe (1991), and Muntean and Einaudi (2001). Here, only a brief compilation is provided.

The basement in northern and central Chile is supposed to consist of discrete fragments of Precambrian to early Paleozoic age belonging in part to the former Gondwana supercontinent (Davidson and Mpodozis, 1991; Vila et al., 1991). There is evidence for an early continuous Carboniferous magmatic arc ranging at least from Copiapó in the north to Coyhaique in the south (Davidson and Mpodozis, 1991). Permian to Triassic rocks are widespread along the northern Chilean territory (Breitkreuz et al., 1989), however, there are only small exposures of Paleozoic to late Triassic basement comprising mainly Devonian to Carboniferous clastic sedimentary sequences in the Maricunga belt. The basement is folded and faulted in a basin-and-range style, with north-to southeast-trending segments variably exposing late Paleozoic, mid-Miocene, and late Triassic to Cretaceous rocks (Vila and Sillitoe, 1991). Reversed faults were installed in the upper Cretaceous (Mpodozis et al., 1995) and form in particularly the western border of the belt with displacements of up to 700 m (Vila and Sillitoe, 1991). The north to north-northeast trending tectonic pattern as well as a subordinate northwest pattern are well expressed in almost all major hydrothermal alteration zones, which are part of the spatially more restricted gold deposits and prospects (Fig. 2).

During late Cretaceous to mid-Eocene, magmas erupted in the Precordillera at the latitude of Copiapó, but they only crop out in the surroundings of Volcán Copiapó, Nevado de Jotabeche and in the La Coipa area (Mpodozis et al., 1995, Fig. 2). No magmatic activity occurred directly in the Maricunga belt in late Eocene, but is noticed west of the belt. In this phase a second tectonic pattern with northwest orientation was developed. These faults were reactivated in late Oligocene and Miocene (Mpodozis et al., 1995). The early Oligocene was a time of magmatic quiescence; only a few porphyry intrusions were emplaced in the central part of the belt (Mpodozis et al., 1995).

The dominant rocks within the Maricunga belt are of mid-Oligocene to Pliocene age and can be subdivided into five discrete chronological units (González-Ferrán et al., 1985; Mpodozis et al., 1995, Fig. 2). Most of these magmatic-tectonic episodes coincide with phases of mineralization and alteration. The first episode from late Oligocene to early Miocene (26–21 Ma) was initiated by the breakup of the Farallon plate (Sillitoe et al., 2013). Magmatic activity took place in the northern and southern part of the belt culminating in the eruption of the Cerros Bravos and Barros Negros stratovolcanoes, the Esperanza and La Coipa dacitic dome clusters and small dome complexes in the domains of La Pepa, Maricunga Mine, Pantanillo and Santa Cecilia. All these volcanic centers are host to contemporaneous gold mineralization and are

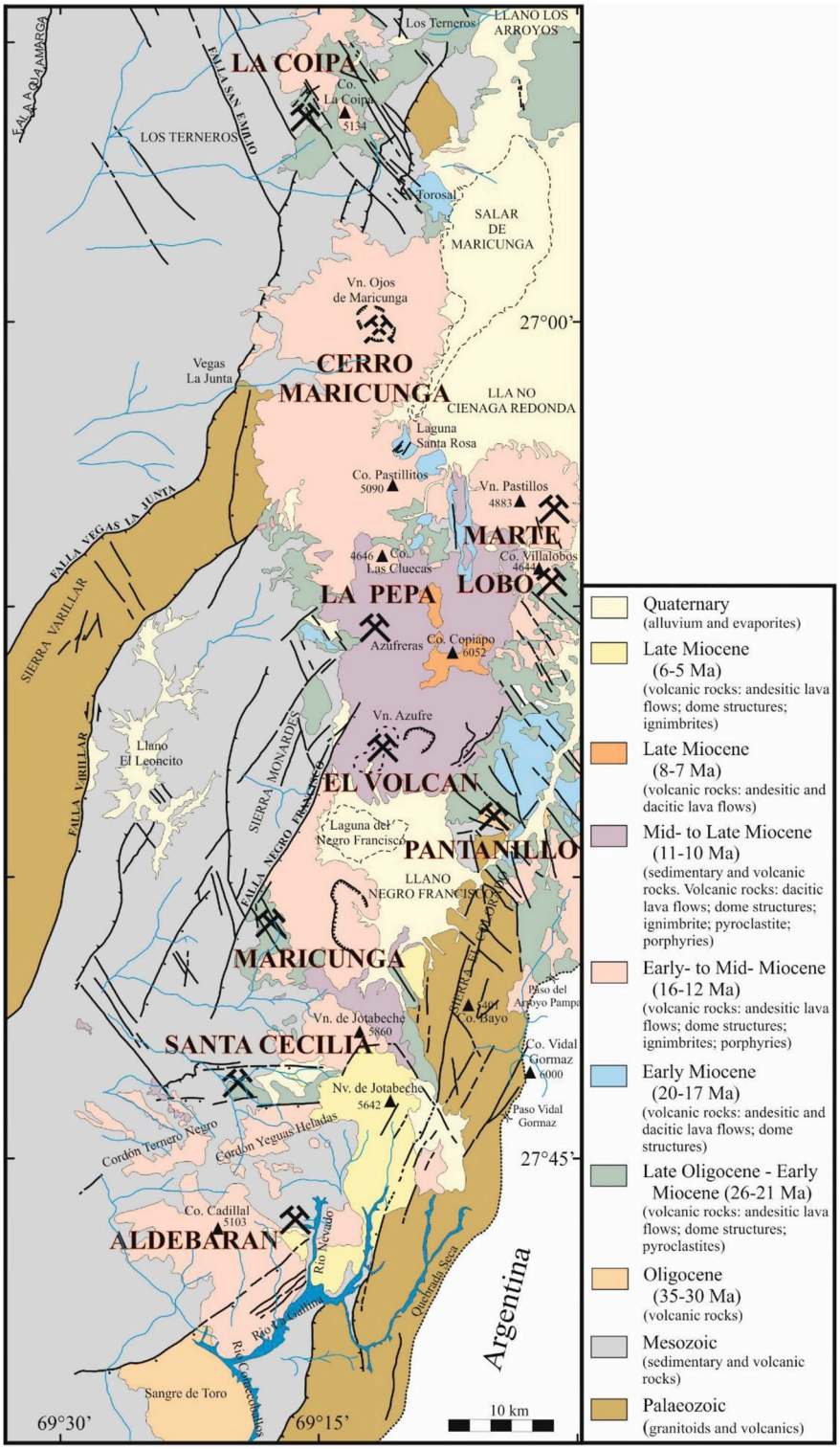


**Fig. 2.** The Cerro Maricunga gold prospect is part of the central part of the Maricunga gold belt, whose Oligocene to Miocene igneous rocks are host to transitional porphyry-epithermal gold (-silver) deposits (simplified after Mpodozis et al., 1995). (For interpretation of the references to color in this figure legend, the reader is referred to the Web version of this article.)

related to northwest to west-northwest oriented fault systems (Mpodozis et al., 1995). The second episode relates to the early Miocene (20–17 Ma) and presents an amagmatic time characterized by compressional deformation and crustal thickening (Mpodozis et al., 1995). This quiet time is followed by the magmatically most active episode in the whole belt, when between 16 and 12 Ma several voluminous stratovolcanoes were constructed under more extensional conditions, including Cadillal, Doña Inés, Jotabeche Norte, La Laguna, Santa Rosa, Villalobos and the most outstanding one at Ojo de Maricunga (Davidson and Mpodozis, 1991). To the end of this time span the gold porphyries in the Lobo, Marte, Escondida and Aldebarán domains were emplaced, but generally magmatic activity diminished and was afterwards restricted to Volcán Copiapó during the fourth episode from 11 to 7 Ma (Vila et al., 1991; Mpodozis et al., 1995). The transition to the

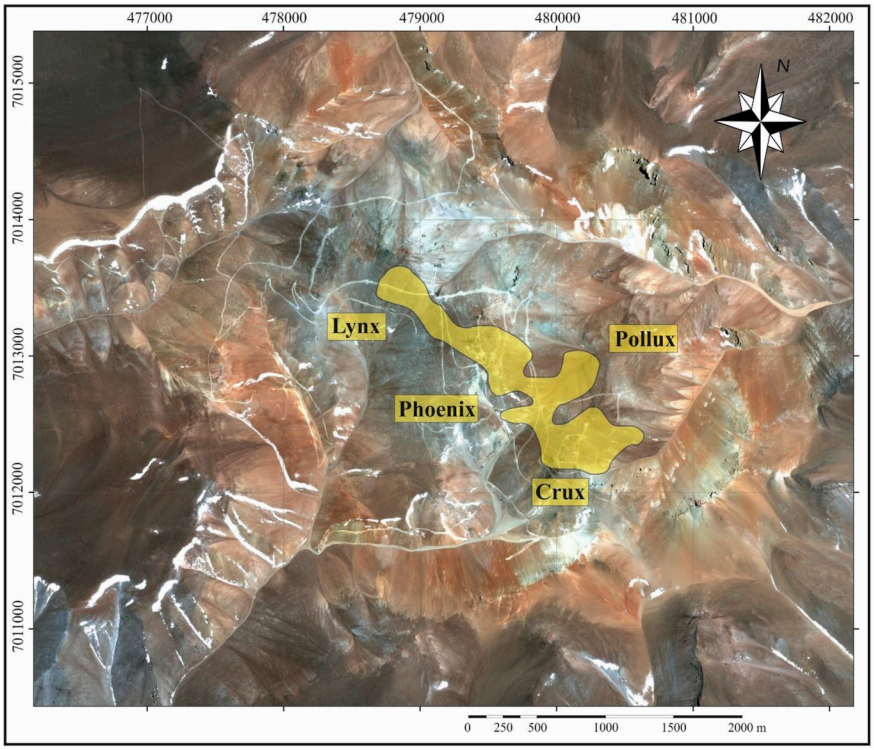


**Fig. 3.** Satellite image showing the currently identified zones of mineralization: Crux, Lynx, Phoenix and Pollux inside the inner part of the partially eroded Ojo de Maricunga volcano. The yellow area marks the approximate outline of gold mineralization that is related to the strongly eroded interior zone of the volcano. The reddish zone is suggestive of argillic alteration and formation of limonite, and passes into propylitic alteration in the surroundings (taken from Lohmeier et al., unpublished results, a). *2-column fitting image; colored, online only.* (For interpretation of the references to color in this figure legend, the reader is referred to the Web version of this article.)

contemporary magmatic lull took place with decreasing magmatic activity in late Miocene to Pliocene (6–5 Ma) when magmatic activity was limited to the Nevado de Jotabeche in the south of the belt (Mpodozis et al., 1995).

## 3. Material and methods

The sample material is from exploration work during the field season 2010/2011. After intense trench mapping and detailed core- and cutting (re-)logging of more than 70 drillings, in total 234 samples (82 drillcore, 69 drillcore-pulp, 69 trench, 14 bulk-trench pulp samples) were taken, covering the known mineralized zones at that time. Each drillcore-pulp sample represents a drillcore interval of two meters, each bulk-trench pulp sample a trench interval of five meters. The majority of drillcore samples was taken from deeper levels in order to avoid more advanced weathering effects. Sampling of unaltered rocks was impossible due to pervasive, albeit weak, intermediate argillic alteration.

Parallel to geochemical analysis, petrographic on-site characterization was completed and improved by microscopic analysis of more than 80 polished thin sections and by geochemically based rock discrimination.

Solid drillcore and trench samples were split into two halves, one for polished thin and thick section preparation, the other, after crushing and grinding, for chemical analysis. Petrographic work in transmitted and reflected light was completed by electron microprobe analysis (EMP; Technical University of Clausthal, Germany), cathodoluminescence imaging (CL; Johannes-Gutenberg University of Mainz, Germany), and laser ablation - inductively coupled plasma - mass spectrometry (LA-ICP-MS; GeoZentrum Nordbayern, Germany). Bulk-rock chemical analysis of the major elements and most trace elements was by a combination of inductively coupled plasma optical emission spectrometry (ICP-OES) and inductively-coupled plasma mass spectrometry (ICP-MS) after lithium metaborate/tetraborate fusion followed by dilute nitric acid digestion. Aqua regia digestion was used for analysis of precious and base metals; additional trace elements were analyzed after four-acid digestion. This analytical work was done by AcmeLabs (Canada). Crushed rock splits were used for U-Pb dating at the Karpinskii All-Russian Geological Institute of Geology (VSEGEI) in Saint-Petersburg (Russia), where also ten bulk rock powders were analyzed for Sm-Nd isotope composition. Oxygen and sulfur isotope analyses of sulfate and sulfide mineral separates were done at the Westfälische Wilhelms University of Münster (Germany). Details of the analytical methods are provided in ESM (electronic supplementary material) part A. All analytical results are shown in ESM part B.

The sample suite is supplemented by 14 samples from Hochschild's El Volcán project, taken during the field season 2007/2008 when the project was still in possession of the Chilean subsidiary of the Canadian based company Andina Minerals. The same wet-chemical analytical methods were applied.

The Nd isotope composition and the Sm and Nd concentrations were determined by isotope dilution using a solid-state multi-collector mass-spectrometer TRITON Ti (Thermal Electron) in static mode at the VSEGEI. The samples were spiked with a $^{150}$Nd-$^{149}$Sm mixed isotopic tracer and the elements were extracted according to the conventional method of chromatographic separation (Richard et al., 1976). The analytical errors (2σ) were about 0.3% for $^{147}$Sm/$^{144}$Nd and ≪0.005% for $^{143}$Nd/$^{144}$Nd. The analytical errors in the concentrations of the elements are 0.5–1%. The reproducibility of the analytical data was checked by measuring international standards such as La-Jolla, BCR-1, 2, SRM-987. The $^{143}$Nd/$^{144}$Nd ratio for the Nd standard JNdi-1 during the experiments was 0.512112 ± 5. The laboratory blanket was less than 0.01 ng for Nd and Sm. $\varepsilon_{Nd}$ T values were calculated for 10 Ma and 20 Ma.

Zircons were extracted by conventional separation techniques from one composite rock sample including core material of different depths from the drillings CMD001, CMD008, CMD009, CMD014, CMD016, CMD026, CMD027, and CMD037. U-Pb zircon dating on 37 grains was carried out on the SHRIMP II ion microprobe at VSEGEI. A primary beam of molecular oxygen was employed for zircon ablation. The analytical spots had a size of about 27 × 20 μm, and the corresponding primary ion current was about 4 nA at 10 kV. Mass-resolution was M/ΔM > 5000 (1% valley) so that all isobaric interferences were resolved. The following ion species were measured in sequence: $^{196}Zr_2O$ - $^{204}$Pb - background (~204.5 AMU) - $^{206}$Pb - $^{207}$Pb - $^{208}$Pb - $^{238}$U - $^{248}$ThO -

$^{254}$UO with integration time ranging from 2 to 20 s. Four cycles for each analysis were acquired. Each fifth measurement was carried out on the TEMORA 1 zircon U/Pb standard (Black et al., 2003). The 91500 zircon (Wiedenbeck et al., 1995) was applied as standard for U concentration. The results were processed with SQUID v1.13a (Ludwig, 2005a) and ISOPLOT/Ex 3.22 (Ludwig, 2005b) software, using the decay constants of Steiger and Jäger (1977). The common lead correction was done using measured $^{204}$Pb according to the model of Stacey and Kramers (1975).

## 4. Results

### 4.1. Petrography

The Cerro Maricunga area was first mapped by Mpodozis et al. (1995) as volcanic rocks composed of andesitic to (rhyo)dacitic composition of early to mid-Miocene age. The exposed volcanic edifice of volcano Ojo de Maricunga is largely composed of pyroclastic flow deposits. The central crater comprises a dacitic dome which is broadly surrounded by abundant ignimbrite layers as relics of initial volcanic activity (Mpodozis et al., 1995). Our data (fieldwork, core and cutting mapping, microscopic and in particular geochemical analysis) indicate that the bulk of the igneous rocks is of andesitic composition (Figs. 4 and 5; Table 1). There is a wealth of different breccia types, including magmatic, phreatic and phreatomagmatic breccias, mostly polymictic, all likewise of andesitic bulk composition. The same applies to pyroclastic rocks, comprising ignimbrites, litho-crystal tuffs and crystal tuffs. The rock suite is completed by tuffisite and pebble dikes. Rock types of non-andesitic composition are rare. They comprise daciandesitic porphyries and flows as well as (glomero)porphyritic dacites locally affected by silicification. All samples, irrespective of their classification, are variably overprinted by intermediate argillic alteration. Several samples show a late metasomatic overprint with hydrothermal formation of clinopyroxene and chlorite. A detailed (microscopic) documentation of the different rock types can be found in ESM part D.

#### 4.1.1. Igneous rocks

Almost all igneous rocks, irrespective of whether they are developed as flows, porphyries or dikes, share a quite similar petrographic signature, but diverging texture (Figs. 4 and 5). Whereas flows show a porphyritic texture with aligned phenocrysts set in a (mostly) pervasively argillic altered, formerly microcrystalline groundmass with flow or microcrystalline equigranular texture, porphyries express a pronounced porphyritic or glomerophyritic texture with a former microcrystalline ± equigranular groundmass. Dikes are characterized by a clear flow texture. The contacts to the wall rocks are sharp. In places, small oriented feldspar laths display a subparallel alignment. Alternating magma pulses are discernible by flow bands of mm to meter scale.

The phenocryst mineral suite encompasses primarily plagioclase and variable amounts of altered clinopyroxene, late magmatic magnetite, and accessory orthopyroxene (enstatite) and quartz. Hornblende rarely occurs and is only observed in flows. Locally, two to three different phenocryst generations can be distinguished.

Plagioclase is by far the most abundant phenocryst phase within the Cerro Maricunga rock suite. The crystals are widely characterized by a compositional oscillatory or patchy zoning (see ESM part D). Compositions of single crystals change mostly from oligoclase ($An_{25}$) to bytownite ($An_{80}$) or simply within the andesine field ($An_{30}$–$An_{45}$). Plagioclase has rims with widths of 10 to > 1000 µm, without any preference to more calcic or more sodic compositions to larger or smaller bandwidths. Plagioclase microlites display in part a normal zoning, but frequently no zoning is discernible. The plagioclase crystals show both reverse and normal zoning, mainly expressed as step zoning, although sometimes a progressive zoning is distinguishable in single shells. Patchy zoning of plagioclase crystals is infrequent. It is displayed by skeletal crystals of oligoclase composition, entrapped and overgrown by labradorite during changed growth conditions. Sieve textures are rare, and are likely the result of alteration. Few crystals show trails of melt inclusions. K-feldspar is characterized as sanidine. Hypidiomorphic and fragmental plagioclase and K-feldspar crystals are widespread. Euhedral and glomerocrystic plagioclase is abundant in porphyries, but rare in flows and dikes.

Almost all clinopyroxene crystals belong to the diopside-hedenbergite solid-solution series (EMP analysis; ESM part D). Some are diopsidic augite, but with clear tendency towards more calcic composition. Similar to plagioclase, some clinopyroxene crystals have melt inclusions.

Apatite is present at Cerro Maricunga in two forms: fluorapatite and chlorapatite. Hypidiomorphic, but mostly anhedral or equant fluorapatite crystals relate to the groundmass and belong to the primary magmatic mineral suite. The same applies to rare apatite-needles enclosed in feldspar. In contrast, the second generation of anhedral apatite crystals pertains to chlorapatite and is clearly post-magmatic, growing in interstices and secondary voids.

Quartz has mainly anhedral to fragmental shape, but in addition, corroded crystals with an irregular curved and partly embayed shape are present. These individual corroded and glomerocrystic quartz aggregates are a conspicuous feature in particularly in (glomero)porphyritic rocks. The “quartz eyes” with sizes of up to 1.5 cm (see ESM part D) have in part a cellular, in part a spherulitic or globular internal texture, not attributable to micro-fissures. Some show a uniform, others a patchy extinction. Several crystals, including individual ones, show zones of light and darker grey color under CL indicating an inhomogeneous trace element distribution. Some quartz eyes exhibit an irregular and in part a sectoral zoning under CL reflecting rapid growth. Common are curved fissures cutting quartz eyes. Fluid inclusions from overprinting hydrothermal fluids are rare. The crystals have largely clear contours, but few show scraggy rims pointing to a corrosion event. Frequently, quartz eyes served as nucleus during later hydrothermal overprint reflected by surrounding bright, fuzzy rims under CL. Indications for a second crystallization event following the formation of the cores are rare.

Rarely, small gabbroic xenoliths and crystal clots occur. Besides altered clinopyroxene and plagioclase, they consist of a large proportion of up to 40% magnetite-ilmenite. The amount of plagioclase is lower in the xenoliths and in the clots than in the bulk rock assemblage. Whereas gabbroic xenolith are composed of closely interlocked material, subhedral shapes of most clot minerals give the clots a microporphyritic texture. A special kind of xenoliths are distinctly altered rock fragments with cross-cutting B-veinlet quartz. Polymict andesitic fragments are rare.

#### 4.1.2. Volcaniclastic rocks

Ignimbrites surround the upper part of the remnant edifice of the Ojo de Maricunga volcano covering igneous rocks and breccias. They are the only rock type without hydrothermal overprint, suggesting post-hydrothermal emplacement at the end of the volcanic activity at the Ojo de Maricunga volcano. The ignimbrites are internally layered, porous and non-welded. (Sub)rounded former gas-vesicles of up to a few mm size are oriented parallel to the bedding and indicate a former porosity of up to 10%. Larger crystals are embedded and aligned in an equigranular, fine-grained mainly fragmental matrix. Both larger crystals and the fine-grained fraction reflect an andesitic composition.

Litho-crystal tuffs are characterized by subrounded clasts of a few mm to several cm size embedded in an igneous, porous (pore cavity ≤15%), pervasively altered matrix of inhomogeneous texture. A pyroclastic layering or bedding is apparent in the field. Crystals have predominantly fragmental shape indicating an explosive (pre)depositional event. Some samples show a large proportion of glomerocrystic plagioclase or rounded feldspar. At least three different clast types can be distinguished, including porphyritic latites, andesitic flows and

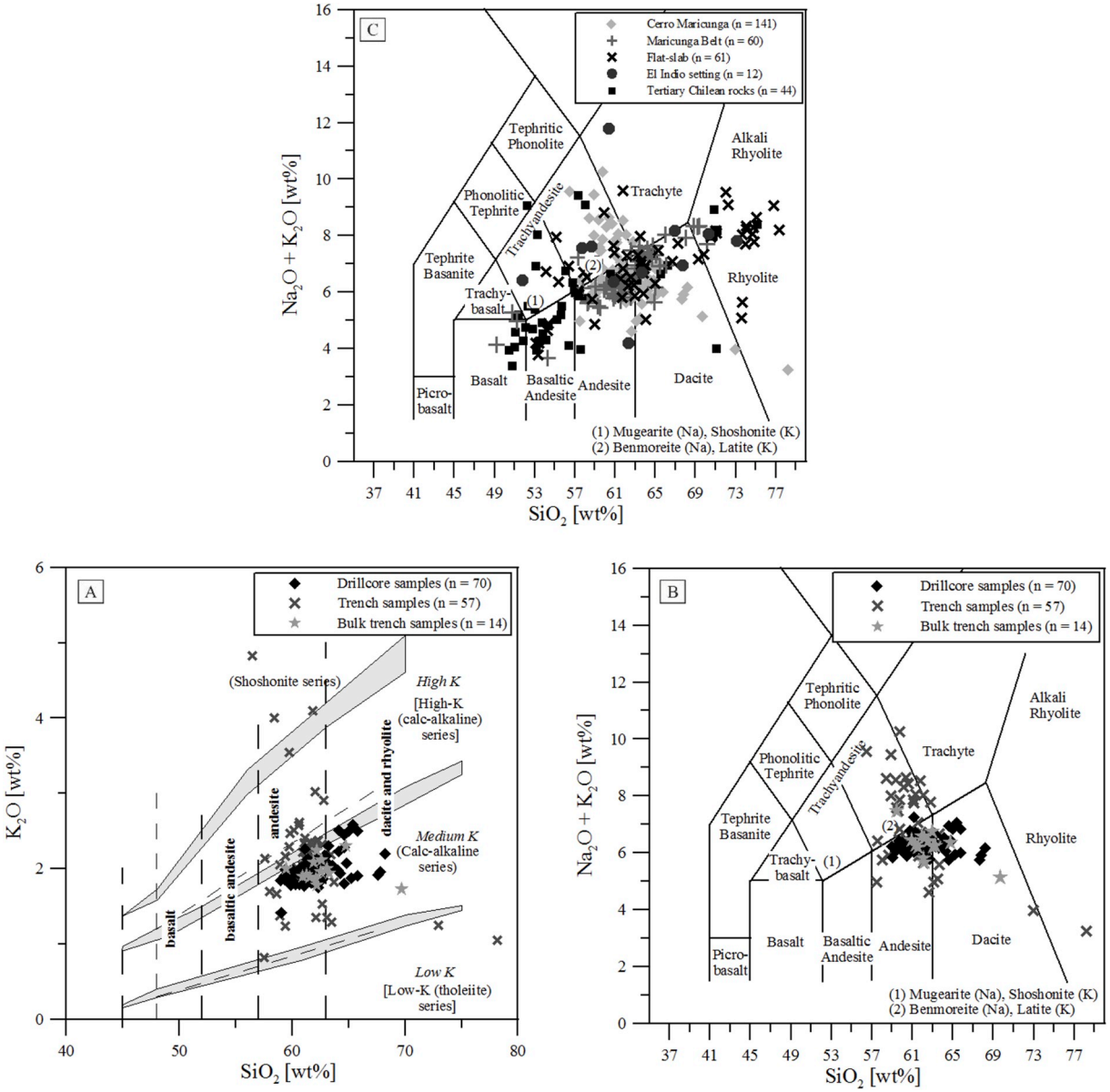


**Fig. 4. A**: Cerro Maricunga rocks are mainly andesite and rarely dacite of the medium-K calc-alkaline series in the $K_2O$ vs silica diagram for subalkalic rocks (with subdivisions of Le Maitre et al. (1989: broken lines with nomenclature in italics) and Rickwood (1989: nomenclature in parentheses)). Although some near-surface trench samples relate apparently to the low-K tholeiitic or high-K calc-alkaline series, this is only due to metasomatic overprint. Likewise, the discrimination as dacite is largely by reason of locally restricted incipient silicification. **B**: The same pattern results using the TAS diagram of Le Maitre et al. (1989). **C**: In the framework of Tertiary Chilean rocks, Cerro Maricunga rocks fit well into the calc-alkaline setting of that time. Data taken from: Maksaev et al. (1984); Kay et al. (1987, 1988, 1994b, 1996, 1999); Mpodozis et al. (1995); Tittler (1995); Hollings et al. (2005).

gabbros.

A group of “crystal tuffs” relates to the coarse-grained (glomero) porphyritic andesites. The main difference to the porphyries is by a local, probably intergranular porosity. Nonetheless, a secondary porosity provoked by post-depositional fluids cannot be excluded. Alteration is generally more advanced compared to the other volcaniclastic rocks. Alternating layers of phenocrysts of different sizes indicate eruptive deposition. Quartz eyes are abundant.

### 4.1.3. Breccias

Polymictic breccia bodies up to several tens of meters wide are abundant. Frequently, fluidization effects and/or juvenile fragments are observed in the field and in drillcore leading to their interpretation as phreatic and phreatomagmatic breccias (Fig. 6). The breccias have a chaotic texture without alignment, layering and sorting. Subrounded clasts of andesitic composition of mono- and polymictic character are abundant. In addition, pervasively silicified and/or chloritized clasts as well as rare latitic clasts are present. Clasts containing fragments of A-veinlets (quartz veinlets with granular texture formed early during the development of a magmatic-hydrothermal system) and B-veinlets (color-banded quartz veinlets formed late in a magmatic-hydrothermal system by flashing during transitions from lithostatic to hydrostatic pressures; Gustafson and Hunt, 1975; Muntean and Einaudi, 2001) occur locally. Polymictic clasts composed of andesitic and gabbroic proportions are rare. The primarily fragmental matrix reflects a primary andesitic composition affected by pervasive alteration. Monomictic breccias with (sub)rounded fragments of andesitic porphyry represent only a minor proportion of the rock suite. In outcrops and drillcore intervals they are limited to few meters. Rarely, they straddle 20 m in outcrops.

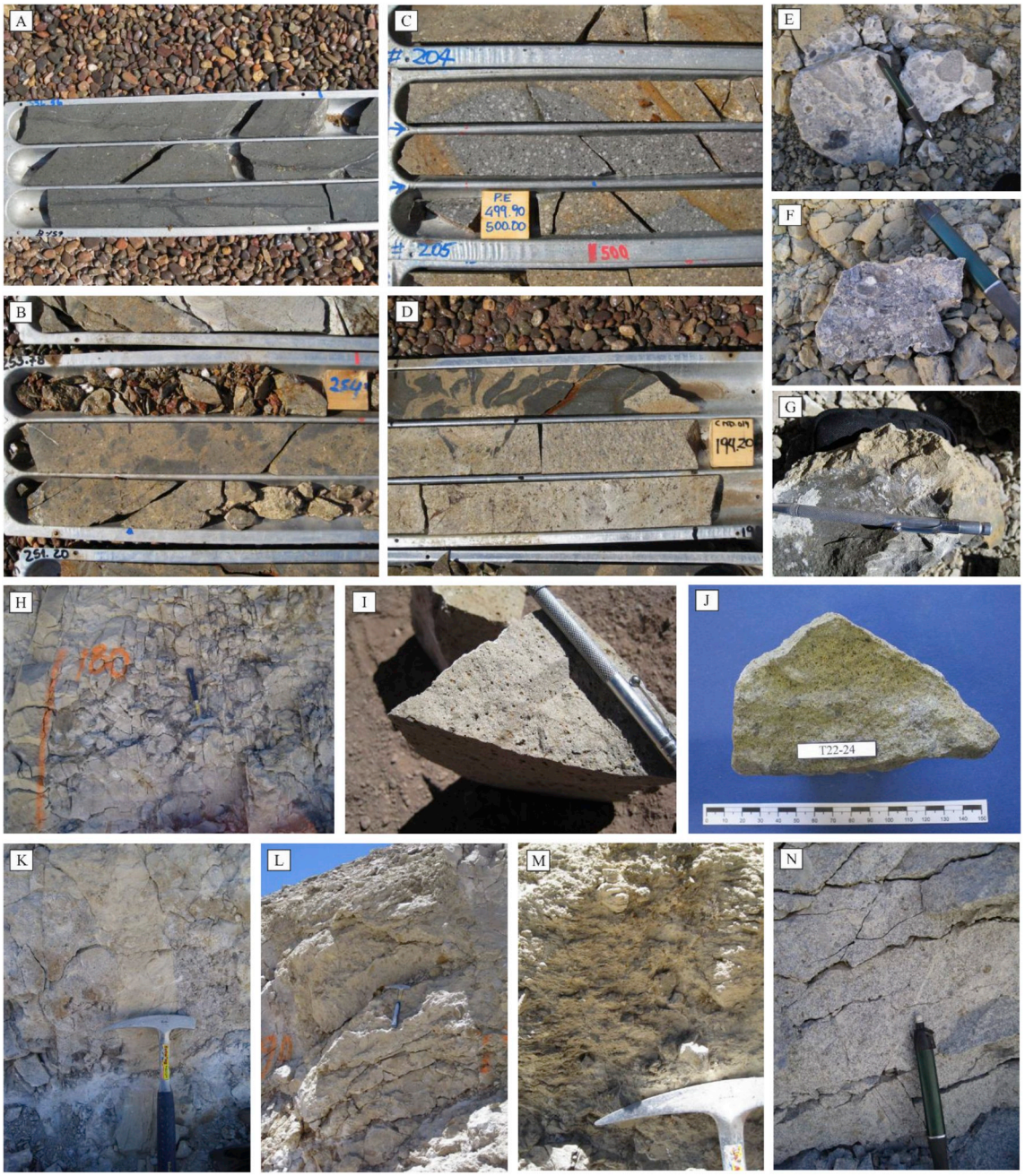


**Fig. 5.** The Maricunga domain encompasses andesitic flows (**A**; drillcore), porphyries (**C**; drillcore) and dikes (**G**: contact dike-monomictic breccia; trench sample). The rock suite is supplemented by crystal tuffs (**N**; trench outcrop), andesitic ignimbrites (**I**; trench sample) and litho-crystal tuffs (**J**; trench sample). Multiple types of breccias occur comprising magmatic (**B**; drillcore), monomictic (**D**; drillcore), magnetite (**H**; trench outcrop) and polymict ones (**E**, **F**; trench samples) which are frequently of phreatic to phreatomagmatic origin. Tuffisite dikes (**K**; trench outcrop) are composed of comminuted material which has macroscopically a clay-like character. They show in places distinct fluidization effects with clastic transport of sulfides and pervasively altered porphyritic and silicified clasts, and elsewhere a rather chaotic transport of material. Tuffisites are widespread and range between few centimeter and 1.5 m in width. They are no shallow phenomenon, rather are documented also at drillcore depth of > 160 m. Overall, the tuffisite material gives the impression of a micro-scale breccia. Pebble dikes (**L**, **M**; trench outcrop) can have a few centimeters in width, but locally up to several meters. They are mostly characterized by (subrounded) to angular and milled fragments set in a clay-like, indistinguishable, unconsolidated matrix. Frequently, pebble dikes show fluidization phenomena, including flow banding, in particular close to straight wall rocks.

Magmatic breccias have an igneous matrix reflecting in part a porphyritic flow texture. Locally, aligned larger hypidiomorphic and fragmental crystals are set in a microcrystalline matrix, but largely a chaotic texture prevails. Locally, alternating flows are distinguishable, and fluidization textures are observed. Indications for several generations of reprocessed igneous material of andesitic bulk composition are present. Various fragments, including mainly porphyritic andesites, but also daciandesites, dacites, and gabbros were assimilated.

Some breccias are conspicuous due to an exceptionally dark color. They are quite porous and pervasively argillic altered with a replacement mineral suite dominated by extremely dark phyllosilicates, primarily characteristic clay minerals of intermediate argillic alteration suites (e.g. kaolinite, illite). First analysis suggests vermiculite as trigger for the dark color (Lohmeier et al., unpublished results, a). The dark phyllosilicates occur particularly within the matrix and are less abundant within clasts. Primarily magmatic magnetite intergrown with ilmenite is concentrated in local accumulations within clasts, but small iron oxide minerals occur also randomly distributed within the matrix.

Field observations show that the formation of these breccias is directly linked with metasomatic overprint.

Tuffisites are widespread in the study area. They can range between a few cm and ~1.5 m in width, and are also seen at drillcore depths > 160 m. Tuffisites are composed of comminuted material of clay-like character in the field (Figs. 5 and 6). They show distinct fluidization effects, along with sorting and alignment, and in places clastic transport of both porphyritic and silicified clasts and of sulfides. Locally, also a chaotic transport of material is demonstrated. Although the clay-like character can be a primary feature (e.g. Taylor, 2009), considerable post-depositional argillic overprint is likely. Generally, tuffisites within the study area give the impression of a micro-scale breccia. Tuffisitic dikes are clearly syn-hydrothermal.

Pebble dikes are likewise widespread. They can have a few centimeters in width, but locally reach up to several meters. In contrast to tuffisites, pebble dikes are only observed in trench outcrops and not in drillcore (Fig. 5). In the field, they are characterized by mm-to cm-sized, (sub)-rounded to rare angular and milled fragments, mainly set in a clay-like, unconsolidated matrix (Fig. 5). In general, fragments share only a minor proportion of the dikes, achieving at most 50%. Frequently, pebble dikes show fluidization phenomena, like flow banding, in particular close to straight wall rocks, and locally shattering and exfoliation of fragments. Fault- or fracture-control can neither be proven nor be ruled out. Pebble dikes are transected by tuffisites and vice versa and are therefore placed at the waning stages of the hydrothermal system.

### 4.2. Geochemistry

The bulk of the Cerro Maricunga rocks is classified by mineralogy and whole-rock geochemistry as andesite and rarely as daciandesite or dacite. All samples are affected, to variable degree, by post-depositional fluid overprint. All Cerro Maricunga rocks are derived from subduction-related arc magmas, pertaining to the (medium-K) calc-alkaline series (Fig. 4). They are geochemically clearly discriminated as andesite, although there is scatter due to alkali and (limited) silica mobility, which is obviously larger concerning trench samples than drillcore samples due to supergene/weathering processes. This effect is minimized by selecting the freshest accessible samples from outcrop, but could not be avoided. Notwithstanding its texturally destructive character, argillic alteration is an in-situ alteration without significant removal and/or supply of alkali elements and thus not expressed in alkali-based discrimination diagrams. The same applies to locally restricted incipient silicification. However, metasomatic fluids changed the bulk rock composition considerably by supplying alkali elements, reflected in the TAS diagram by a tendency towards trachyandesite (Fig. 4). Set in the larger framework of Tertiary Chilean rocks, the Cerro Maricunga rocks fit well into the calc-alkaline setting of that time (Fig. 4).

The affiliation of all rocks to the same igneous domain is underlined by the unimodal frequency distributions of main and minor elements, generally used to separate different populations (Fig. 7). Taking CaO as an example for major elements, a straight unimodal distribution is shown. The same applies for Ba as trace element and also for REE (rare earth elements) represented by La and Ce. Assuming strong silicification or other advanced alteration styles/overprint of individual rocks or rock formations, these should be displayed in frequency plots as separate populations (distinct bends within the range of one standard deviation (1σ)). However, no curved trends are shown by the cumulative frequency distribution of neither $SiO_2$ nor $K_2O$, which would reflect silicification or metasomatic overprint, respectively. Only little dispersion is shown within the range of two second standard deviations (2σ).

Using the $SiO_2$ content as index of differentiation, major elements show a scatter distribution for surface samples and some linear variation trends for drillcore samples in Harker diagrams (Fig. 8). Negative linear variation is apparent in drillcore samples for $TiO_2$, $Al_2O_3$, CaO, MgO, and maybe $Fe_2O_{3,TOT}$ reflecting a differentiation trend from andesite over daciandesite to extremely rare dacite. Local incipient silicification may increase the scatter. However, considering the spread from 60 to 68 wt% $SiO_2$ (with an average of ~63 wt%), these trends with changes in Ti, Al, Ca and Mg are likely due to magmatic fractionation. Metasomatic overprint causing an excess of alkali elements is displayed in the $SiO_2$ vs ($Na_2O$ + $K_2O$) plot, concealing a clear magmatic trend.

The Cerro Maricunga samples show steep REE patterns with respect to LREE/HREE (light rare earth elements/heavy rare earth elements) fractionation and have a relatively flat HREE distribution, when chondrite-normalized (Fig. 9). The steep and spoon-like REE patterns of Cerro Maricunga are indicative of garnet and/or amphibole in the magma source due to preferential partitioning of HREEs into garnet and amphibole, whereas MREE (middle rare earth elements) partitioning is favored in amphibole. In this context, the REE patterns suggest magma formation at a transitional stage when a hornblende-garnet bearing residuum passed over into a garnet residuum.

Compared with some data from the neighboring El Volcán deposit, there is an overlap, but in general, the concave-upward curvature of the Cerro Maricunga REE pattern is less pronounced. This relation is even more apparent considering the steep REE patterns of the Miocene porphyry-Cu deposit Los Pelambres in Central Chile, whereby Los Pelambres formed in thick evolved crust (Fig. 9). Likewise, Cerro Maricunga was formed within a setting of thick continental crust, where the magma source might be located at depths of ≥45 km and thus in the garnet-stability field.

Considering trace element fingerprints, the typical subduction-related arc-signature is apparent with enrichment in LIL (large-ion lithophile) elements relative to HFS (high-field-strength) elements and thus for the HFSEs Nb, P, Ti, but not for Zr (Ulmer, 2001). In addition, the HREEs Tb, Yb und Lu are enriched (Fig. 10). Shown in N-MORB normalized Spider diagrams negative anomalies of Ta, Nb, P, Hf, Ti, Y, Yb and Lu are distinguishable indicating an enriched sub-continental lithosphere source (Ta, Nb, Hf; Pearce, 1983) and the formation of Cerro Maricunga during a phase of thickened crust (Y, Yb; Fig. 10) with garnet and/or amphibole present. Comparing Cerro Maricunga samples with Andean adakite-like high-Mg andesite samples a remarkable similarity is given (Fig. 10).

### 4.3. U-Pb dating of zircon

We obtained 37 U-Pb ages on zircon from a composite drillcore sample (Table 2). About half of these ages are older than the stratigraphic age of the Cerro Maricunga sequence. The $^{206}Pb/^{238}U$ ages encompass a very broad age spectrum from Neoproterozoic (694 ± 9 Ma (2σ)) over Permian (259 ± 5 Ma to 254 ± 9 Ma) and Triassic ages (247 ± 5 Ma) to Paleogene (64.4 ± 1.6 Ma to 28.6 ± 1.2 Ma) and Neogene ages (23.5 ± 1.7 to 14.9 ± 0.9 Ma; Table 3). Paleogene ages relate to Paleocene (64.4 ± 1.6 Ma to 61.3 ± 2.2 Ma) and Oligocene (31.6 ± 1.5 Ma to 28.6 ± 1.2 Ma), Neogene ages to early (23.5 ± 1.8 Ma to 16.1 ± 0.4 Ma) and mid-Miocene (15.9 ± 0.8 Ma to 14.9 ± 0.9 Ma). Some Permian and Paleocene zircon cores possess overgrowth of early Miocene age (Fig. 11). It is particularly interesting that there is a continuous age spectrum from ~32 to 15 Ma, including the proposed near magmatic lull from 20 to 17 Ma (Mpodozis et al., 1995; Kay et al., 1999) which is not seen in the Cerro Maricunga area.

### 4.4. Isotope geochemistry

#### 4.4.1. Samarium-neodymium isotopes

Ten bulk-rock samples were analyzed for their Sm-Nd composition (Table 3). The samples are from various drillcores and two trench samples, but have an astonishingly homogeneous composition both in terms of absolute Nd and Sm abundance and in terms of $^{143}Nd/^{144}Nd$ ratio ($^{143}Nd/^{144}Nd$: 0.512434–0.512471). The $\varepsilon_{Nd}$ value is 3.5 ± 0.2

**Table 1**
Selected bulk rock analytical results for Cerro Maricunga samples by ICP-OES (major and minor trace elements after lithium metaborate/tetraborate fusion plus dilute nitric digestion) and ICP-MS (REEs and refractory elements after lithium metaborate/tetraborate fusion and nitric acid digestion; precious and base metals after aqua regia digestion). The full dataset is given in ESM part B.

| | Analyte | $SiO_2$ | $TiO_2$ | $Al_2O_3$ | $Fe_2O_{3,TOT}$ | MnO | MgO | CaO | $Na_2O$ | $K_2O$ | $P_2O_5$ | LOI | $C_{TOT}$ | $S_{TOT}$ | Sum | La |
|---|---|---|---|---|---|---|---|---|---|---|---|---|---|---|---|---|
| | Unit | wt% | wt% | wt% | wt% | wt% | wt% | wt% | wt% | wt% | wt% | wt% | wt% | wt% | wt% | ppm |
| | MDL | 0.01 | 0.01 | 0.01 | 0.04 | 0.01 | 0.01 | 0.01 | 0.01 | 0.01 | 0.01 | −5.1 | 0.02 | 0.02 | 0.01 | 0.1 |
| Drillcore samples | **CMD009–306** | 60.02 | 0.76 | 17.73 | 4.68 | 0.06 | 2.27 | 5.66 | 4.14 | 1.92 | 0.24 | 2.2 | 0.08 | < 0.02 | 99.70 | 23.1 |
| | **CMD014–170** | 62.03 | 0.61 | 16.01 | 4.36 | 0.09 | 1.87 | 4.93 | 4.37 | 2.06 | 0.19 | 3.1 | 0.13 | 0.67 | 99.66 | 25.1 |
| | **CMD014–356** | 59.32 | 0.63 | 16.55 | 4.56 | 0.11 | 2.11 | 5.58 | 4.15 | 1.91 | 0.23 | 4.5 | 0.16 | 1.13 | 99.65 | 22.5 |
| | **CMD014–390** | 61.02 | 0.64 | 17.12 | 4.59 | 0.09 | 2.07 | 4.89 | 4.62 | 2.04 | 0.24 | 2.3 | 0.15 | 0.19 | 99.65 | 24.6 |
| | **CMD016–216** | 61.41 | 0.66 | 17.11 | 4.16 | 0.08 | 1.80 | 4.99 | 4.37 | 2.03 | 0.24 | 2.9 | 0.07 | 0.70 | 99.71 | 23.0 |
| | **CMD019–68** | 61.13 | 0.56 | 16.31 | 3.90 | 0.12 | 3.08 | 4.98 | 5.00 | 2.26 | 0.21 | 2.1 | 0.11 | < 0.02 | 99.69 | 21.6 |
| | **CMD019–118** | 59.64 | 0.78 | 17.94 | 4.84 | 0.08 | 2.15 | 5.81 | 4.61 | 1.81 | 0.25 | 1.8 | 0.09 | < 0.02 | 99.69 | 21.5 |
| | **CMD019–192** | 60.78 | 0.71 | 17.30 | 4.54 | 0.08 | 2.09 | 5.36 | 4.76 | 2.01 | 0.26 | 1.8 | 0.07 | < 0.02 | 99.71 | 21.6 |
| | **CMD026–60** | 60.29 | 0.66 | 17.87 | 4.21 | 0.05 | 1.89 | 5.12 | 4.15 | 1.79 | 0.25 | 3.5 | 0.04 | < 0.02 | 99.74 | 19.8 |
| | **CMD026–238** | 64.11 | 0.55 | 15.59 | 3.90 | 0.07 | 1.63 | 4.64 | 4.01 | 2.51 | 0.19 | 2.5 | 0.13 | 0.26 | 99.68 | 20.0 |
| | **CMD026–264** | 64.58 | 0.54 | 15.14 | 3.88 | 0.06 | 1.65 | 4.72 | 4.10 | 2.28 | 0.18 | 2.6 | 0.11 | 0.31 | 99.73 | 17.6 |
| | **CMD026–352** | 63.55 | 0.66 | 16.60 | 4.30 | 0.06 | 1.88 | 4.89 | 4.13 | 2.04 | 0.24 | 1.3 | 0.06 | 0.04 | 99.64 | 23.0 |
| | **CMD027–222** | 60.63 | 0.50 | 15.78 | 5.08 | 0.06 | 2.27 | 4.27 | 4.43 | 1.79 | 0.20 | 4.7 | 0.17 | 0.40 | 99.74 | 18.0 |
| | **CMD027–228** | 61.06 | 0.53 | 16.20 | 4.61 | 0.05 | 2.41 | 4.09 | 4.42 | 1.77 | 0.22 | 4.4 | 0.13 | 0.31 | 99.72 | 20.2 |
| | **CMD037–42** | 60.65 | 0.69 | 17.14 | 4.55 | 0.07 | 2.08 | 5.31 | 4.23 | 2.00 | 0.25 | 2.7 | 0.04 | 0.08 | 99.71 | 20.3 |
| Trench samples | **T12–7.1** | 60.34 | 0.74 | 17.40 | 4.52 | 0.08 | 2.15 | 5.11 | 4.63 | 1.86 | 0.25 | 2.6 | 0.10 | < 0.02 | 99.71 | 23.3 |
| | **T12–10.1** | 60.52 | 0.69 | 17.54 | 4.26 | 0.05 | 1.95 | 5.48 | 4.27 | 2.00 | 0.23 | 2.8 | 0.04 | 0.08 | 99.76 | 19.7 |
| | **T12–15** | 61.78 | 0.73 | 17.70 | 4.29 | 0.06 | 1.73 | 5.41 | 4.50 | 2.17 | 0.27 | 1.1 | 0.03 | < 0.02 | 99.73 | 22.0 |
| | **T22–1** | 62.17 | 0.61 | 17.42 | 3.61 | 0.04 | 1.60 | 4.62 | 4.10 | 2.30 | 0.23 | 3.1 | 0.04 | < 0.02 | 99.76 | 21.5 |
| | **T22–27.2** | 61.08 | 0.57 | 16.17 | 3.56 | 0.12 | 3.09 | 4.74 | 5.53 | 2.34 | 0.20 | 2.3 | 0.06 | < 0.02 | 99.68 | 20.8 |

| | Ce | Pr | Nd | Sm | Eu | Gd | Tb | Dy | Ho | Er | Tm | Yb | Lu | Y | Rb | Cs |
|---|---|---|---|---|---|---|---|---|---|---|---|---|---|---|---|---|
| | ppm | ppm | ppm | ppm | ppm | ppm | ppm | ppm | ppm | ppm | ppm | ppm | ppm | ppm | ppm | ppm |
| | 0.1 | 0.02 | 0.3 | 0.05 | 0.02 | 0.05 | 0.01 | 0.05 | 0.02 | 0.03 | 0.01 | 0.05 | 0.01 | 0.1 | 0.1 | 0.1 |
| Drillcore samples | 50.8 | 6.38 | 27.6 | 4.59 | 1.24 | 3.11 | 0.42 | 1.88 | 0.33 | 0.87 | 0.13 | 0.78 | 0.12 | 8.9 | 55.3 | 1.7 |
| | 51.7 | 6.28 | 26.3 | 3.97 | 1.14 | 2.72 | 0.41 | 1.94 | 0.40 | 0.99 | 0.16 | 0.94 | 0.15 | 11.0 | 64.8 | 0.8 |
| | 47.8 | 6.18 | 25.7 | 4.10 | 1.21 | 3.06 | 0.43 | 2.25 | 0.40 | 0.95 | 0.17 | 1.23 | 0.15 | 11.1 | 64.3 | 1.5 |
| | 49.7 | 6.04 | 26.1 | 3.92 | 1.10 | 2.93 | 0.39 | 2.06 | 0.40 | 0.95 | 0.16 | 0.92 | 0.15 | 11.0 | 61.0 | 0.9 |
| | 48.1 | 5.85 | 22.8 | 3.79 | 1.07 | 2.65 | 0.38 | 2.01 | 0.38 | 0.98 | 0.14 | 0.93 | 0.14 | 9.5 | 58.4 | 1.1 |
| | 43.1 | 5.37 | 21.8 | 3.43 | 0.90 | 2.20 | 0.31 | 1.55 | 0.28 | 0.73 | 0.11 | 0.70 | 0.10 | 7.4 | 63.2 | 0.5 |
| | 45.7 | 5.63 | 23.7 | 3.90 | 1.13 | 2.91 | 0.39 | 2.03 | 0.35 | 1.00 | 0.14 | 0.86 | 0.14 | 9.7 | 47.3 | 0.9 |
| | 46.3 | 5.83 | 26.1 | 3.92 | 1.15 | 2.73 | 0.36 | 1.85 | 0.30 | 0.77 | 0.12 | 0.74 | 0.10 | 8.8 | 52.5 | 1.3 |
| | 42.9 | 5.23 | 21.3 | 3.50 | 1.04 | 2.59 | 0.37 | 1.93 | 0.33 | 0.92 | 0.14 | 0.83 | 0.14 | 9.1 | 43.9 | 1.6 |
| | 42.3 | 5.18 | 21.2 | 3.43 | 1.03 | 2.42 | 0.33 | 1.74 | 0.25 | 0.71 | 0.11 | 0.75 | 0.12 | 8.3 | 81.3 | 1.0 |
| | 37.0 | 4.73 | 18.0 | 3.27 | 0.92 | 2.44 | 0.30 | 1.18 | 0.28 | 0.53 | 0.12 | 0.43 | 0.11 | 8.2 | 65.7 | 0.7 |
| | 49.7 | 5.94 | 25.1 | 4.07 | 1.12 | 2.64 | 0.36 | 1.81 | 0.29 | 0.87 | 0.13 | 0.87 | 0.11 | 8.6 | 60.1 | 0.9 |
| | 37.3 | 4.54 | 18.7 | 2.93 | 0.80 | 2.01 | 0.25 | 1.22 | 0.22 | 0.53 | 0.09 | 0.62 | 0.08 | 6.5 | 50.8 | 0.7 |
| | 41.0 | 4.83 | 20.8 | 3.00 | 0.84 | 2.23 | 0.28 | 1.34 | 0.24 | 0.58 | 0.10 | 0.77 | 0.09 | 7.0 | 55.5 | 0.8 |
| | 43.8 | 5.49 | 23.8 | 4.02 | 1.06 | 2.61 | 0.37 | 1.67 | 0.31 | 0.93 | 0.13 | 0.79 | 0.12 | 8.6 | 58.6 | 1.1 |
| Trench samples | 50.5 | 6.07 | 26.0 | 4.19 | 1.16 | 2.74 | 0.36 | 1.78 | 0.32 | 0.68 | 0.12 | 0.69 | 0.09 | 8.9 | 55.9 | 1.3 |
| | 43.4 | 5.35 | 23.0 | 3.70 | 1.02 | 2.47 | 0.32 | 1.71 | 0.26 | 0.76 | 0.10 | 0.59 | 0.10 | 8.3 | 55.3 | 1.0 |
| | 46.6 | 5.85 | 23.4 | 4.12 | 1.15 | 2.77 | 0.37 | 1.72 | 0.29 | 0.73 | 0.11 | 0.65 | 0.09 | 8.3 | 63.2 | 1.6 |
| | 44.4 | 5.49 | 22.5 | 3.60 | 0.99 | 2.35 | 0.32 | 1.63 | 0.27 | 0.78 | 0.11 | 0.68 | 0.11 | 7.7 | 65.1 | 1.1 |
| | 44.0 | 5.28 | 21.5 | 3.33 | 0.93 | 2.33 | 0.30 | 1.60 | 0.26 | 0.64 | 0.11 | 0.57 | 0.08 | 7.9 | 65.4 | 0.7 |

**Table 1** (*continued*)

| | Analyte | Sr | Ba | Th | U | Zr | Hf | Nb | Ta | Ag | As | Au | Be | Bi | Cd | Co |
|---|---|---|---|---|---|---|---|---|---|---|---|---|---|---|---|---|
| | Unit | ppm | ppm | ppm | ppm | ppm | ppm | ppm | ppm | ppm | ppm | ppb | ppm | ppm | ppm | ppm |
| | MDL | 0.5 | 1 | 0.2 | 0.1 | 0.1 | 0.1 | 0.1 | 0.1 | 0.1 | 0.5 | 0.5 | 1 | 0.1 | 0.1 | 0.2 |
| Drillcore samples | **CMD009–306** | 739 | 737 | 3.4 | 0.7 | 159 | 4.0 | 7.3 | 0.4 | < 0.1 | 2.6 | 1.0 | < 1 | < 0.1 | < 0.1 | 10.4 |
| | **CMD014–170** | 791 | 720 | 4.3 | 1.1 | 156 | 4.6 | 9.2 | 0.5 | 0.2 | 11.1 | 551 | 1 | 0.1 | 0.7 | 7.5 |
| | **CMD014–356** | 709 | 686 | 4.0 | 1.0 | 156 | 4.3 | 7.6 | 0.4 | 0.3 | 10.9 | 138 | 1 | 0.2 | 0.3 | 8.1 |
| | **CMD014–390** | 744 | 721 | 3.8 | 0.9 | 154 | 4.2 | 8.0 | 0.5 | 0.2 | 3.3 | 384 | < 1 | < 0.1 | 0.3 | 8.1 |
| | **CMD016–216** | 726 | 688 | 4.0 | 1.0 | 153 | 4.1 | 8.1 | 0.4 | < 0.1 | 8.2 | 82.8 | < 1 | < 0.1 | 0.2 | 7.9 |
| | **CMD019–68** | 681 | 708 | 3.4 | 1.0 | 133 | 4.4 | 5.7 | 0.3 | < 0.1 | 1.9 | 130 | 2 | < 0.1 | < 0.1 | 7.2 |
| | **CMD019–118** | 761 | 662 | 3.1 | 0.6 | 150 | 4.4 | 6.9 | 0.3 | < 0.1 | 2.0 | 46.4 | 2 | < 0.1 | < 0.1 | 9.6 |
| | **CMD019–192** | 713 | 689 | 3.4 | 0.7 | 155 | 4.5 | 6.5 | 0.4 | < 0.1 | 4.3 | 122 | 2 | < 0.1 | < 0.1 | 8.8 |
| | **CMD026–60** | 723 | 631 | 3.3 | 0.7 | 143 | 4.3 | 6.1 | 0.4 | < 0.1 | 3.9 | 42.1 | < 1 | < 0.1 | < 0.1 | 9.1 |
| | **CMD026–238** | 644 | 744 | 3.2 | 1.0 | 138 | 3.9 | 7.0 | 0.4 | 0.1 | 6.9 | 860 | 3 | 0.1 | 0.4 | 8.4 |
| | **CMD026–264** | 612 | 650 | 3.0 | 0.9 | 133 | 3.0 | 5.8 | 0.3 | 0.1 | 2.1 | 1016 | < 1 | < 0.1 | 0.1 | 7.5 |
| | **CMD026–352** | 736 | 758 | 3.5 | 0.9 | 151 | 4.1 | 6.9 | 0.4 | 0.2 | 1.6 | 720 | 2 | < 0.1 | < 0.1 | 9.8 |
| | **CMD027–222** | 636 | 708 | 3.4 | 1.0 | 124 | 3.9 | 5.5 | 0.4 | < 0.1 | 2.8 | 99.8 | < 1 | < 0.1 | 0.1 | 6.1 |
| | **CMD027–228** | 700 | 730 | 3.5 | 1.0 | 132 | 4.0 | 5.9 | 0.5 | < 0.1 | 3.0 | 53.5 | 2 | < 0.1 | < 0.1 | 6.7 |
| | **CMD037–42** | 748 | 712 | 3.3 | 0.9 | 144 | 4.4 | 6.7 | 0.5 | < 0.1 | 1.4 | 18.2 | 1 | < 0.1 | < 0.1 | 9.3 |
| Trench samples | **T12–7.1** | 749 | 744 | 3.9 | 0.7 | 165 | 4.6 | 6.9 | 0.4 | < 0.1 | 2.2 | 48.8 | 2 | < 0.1 | < 0.1 | 10.2 |
| | **T12–10.1** | 728 | 697 | 3.2 | 0.7 | 150 | 3.8 | 5.9 | 0.4 | < 0.1 | 3.3 | 169 | < 1 | < 0.1 | < 0.1 | 8.6 |
| | **T12–15** | 790 | 746 | 3.5 | 0.8 | 157 | 4.5 | 7.5 | 0.5 | < 0.1 | 2.0 | 19.6 | 2 | < 0.1 | < 0.1 | 7.9 |
| | **T22–1** | 747 | 746 | 3.8 | 1.0 | 141 | 4.5 | 6.3 | 0.4 | < 0.1 | 3.5 | 48.7 | 3 | 0.8 | < 0.1 | 6.8 |
| | **T22–27.2** | 731 | 759 | 3.5 | 0.8 | 143 | 3.6 | 6.0 | 0.3 | < 0.1 | 4.5 | 78.1 | 2 | < 0.1 | < 0.1 | 6.9 |

| | Cr | Cu | Ga | Hg | Mo | Ni | Pb | Sb | Sc | Se | Sn | Tl | V | W | Zn |
|---|---|---|---|---|---|---|---|---|---|---|---|---|---|---|---|
| | ppm | ppm | ppm | ppm | ppm | ppm | ppm | ppm | ppm | ppm | ppm | ppm | ppm | ppm | ppm |
| | 14 | 0.1 | 0.5 | 0.01 | 0.1 | 0.1 | 0.1 | 0.1 | 1 | 0.5 | 1 | 0.1 | 8 | 0.5 | 1 |
| Drillcore samples | 27 | 22.9 | 23.4 | 0.01 | 0.5 | 16.6 | 2.2 | < 0.1 | 9 | < 0.5 | 1 | < 0.1 | 114 | < 0.5 | 54 |
| | 21 | 319 | 21.9 | < 0.01 | 2.0 | 20.4 | 5.4 | 0.4 | 7 | < 0.5 | 3 | < 0.1 | 83 | 0.5 | 160 |
| | 48 | 136 | 21.3 | < 0.01 | 25.0 | 51.4 | 6.0 | 0.2 | 7 | < 0.5 | 2 | < 0.1 | 83 | 3.3 | 193 |
| | 21 | 181 | 21.5 | < 0.01 | 1.2 | 20.5 | 2.1 | 0.1 | 7 | < 0.5 | 2 | < 0.1 | 89 | < 0.5 | 197 |
| | < 14 | 63.7 | 20.0 | 0.02 | 3.0 | 28.2 | 2.5 | 0.4 | 7 | < 0.5 | 2 | < 0.1 | 84 | < 0.5 | 58 |
| | 21 | 130 | 20.7 | 0.01 | 0.3 | 8.2 | 2.2 | < 0.1 | 7 | < 0.5 | < 1 | < 0.1 | 77 | < 0.5 | 83 |
| | 21 | 24.7 | 22.4 | < 0.01 | 0.6 | 13.0 | 2.5 | < 0.1 | 9 | < 0.5 | < 1 | < 0.1 | 102 | < 0.5 | 48 |
| | 34 | 102 | 21.9 | 0.02 | 1.0 | 28.8 | 3.7 | < 0.1 | 8 | < 0.5 | 1 | < 0.1 | 91 | < 0.5 | 62 |
| | < 14 | 24.1 | 21.7 | < 0.01 | 1.8 | 13.0 | 4.1 | < 0.1 | 8 | < 0.5 | < 1 | < 0.1 | 88 | < 0.5 | 74 |
| | 41 | 425 | 20.3 | < 0.01 | 3.0 | 27.9 | 2.2 | < 0.1 | 7 | < 0.5 | 1 | < 0.1 | 82 | < 0.5 | 159 |
| | 34 | 287 | 18.9 | < 0.01 | 1.0 | 21.0 | 2.3 | < 0.1 | 6 | < 0.5 | 2 | < 0.1 | 92 | 1.3 | 91 |
| | 27 | 314 | 22.0 | < 0.01 | 2.5 | 27.7 | 1.6 | < 0.1 | 8 | < 0.5 | 4 | < 0.1 | 94 | < 0.5 | 56 |
| | 21 | 32.3 | 20.0 | < 0.01 | 2.5 | 25.2 | 1.9 | 0.1 | 6 | < 0.5 | 1 | < 0.1 | 65 | < 0.5 | 188 |
| | 21 | 13.9 | 20.9 | < 0.01 | 2.0 | 17.8 | 2.0 | < 0.1 | 6 | < 0.5 | 1 | < 0.1 | 64 | < 0.5 | 136 |
| | 27 | 127 | 21.2 | < 0.01 | 0.7 | 18.2 | 1.5 | < 0.1 | 8 | < 0.5 | < 1 | < 0.1 | 97 | < 0.5 | 56 |
| Trench samples | < 14 | 58.3 | 22.8 | < 0.01 | 0.4 | 5.4 | 1.9 | < 0.1 | 8 | < 0.5 | 9 | < 0.1 | 116 | < 0.5 | 54 |
| | 21 | 17.3 | 22.2 | < 0.01 | 0.3 | 6.4 | 1.9 | < 0.1 | 8 | < 0.5 | 4 | < 0.1 | 92 | < 0.5 | 26 |
| | < 14 | 71.2 | 22.7 | < 0.01 | 0.3 | 3.6 | 1.7 | < 0.1 | 6 | < 0.5 | 4 | < 0.1 | 92 | < 0.5 | 45 |
| | < 14 | 28.6 | 21.6 | 0.01 | 0.2 | 3.9 | 2.8 | 0.2 | 7 | < 0.5 | 5 | < 0.1 | 83 | < 0.5 | 65 |
| | < 14 | 34.5 | 20.7 | 0.02 | 1.7 | 2.7 | 0.9 | < 0.1 | 6 | < 0.5 | 6 | < 0.1 | 80 | < 0.5 | 125 |

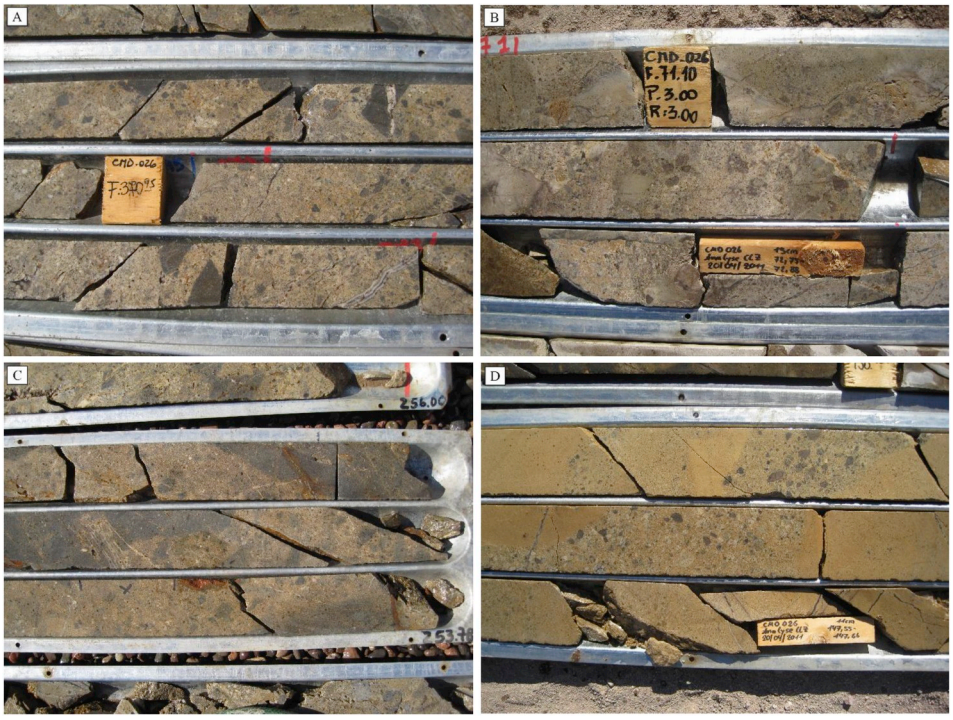


**Fig. 6. A–C**: Argillic altered phreatomagmatic breccias within the Cerro Maricunga area have polymict character. They are matrix-supported and contain a wealth of juvenile fragments as well as single and polyclastic (daci)andesitic and dacitic clasts (**C**). These clastic rocks are cut by mineralized quartz veinlets (B-veinlets; **A**) and contain veinlet clasts giving evidence for multiple-stage, syn-mineral brecciation. **D**: Tuffisite dikes are composed of comminuted material that has macroscopically a clay-like character. They show distinct fluidization effects and in places clastic transport of sulfides and pervasively altered porphyritic and silicified clasts. Sometimes a rather chaotic transport of material is shown.

(n = 10), and the depleted mantle model age for 20 Ma is 981 ± 30 Ma (n = 10). These data suggest significant involvement of Neoproterozoic lower crust in the evolution of the Cerro Maricunga rocks.

The involvement of a larger portion of a lower crustal component in andesites between 25.5°S and 28°S is shown by Kay et al. (2014) by the trend from $^{143}Nd/^{144}Nd$ ratios of 0.51284 in primitive Segerstrom basalts to ± 0.51263 in > 20 Ma andesites of the southern Maricunga belt to ± 0.51255 in < 20 Ma andesites of the southern Maricunga belt to ± 0.51245 in the late Miocene Volcan Copiapó complex. With the Cerro Maricunga $^{143}Nd/^{144}Nd$ ratios in the range of Volcan Copiapó ratios, which formed over a thick crustal keel (Kay and Mpodozis, 2002). However, the rocks can likewise partially originate from forearc

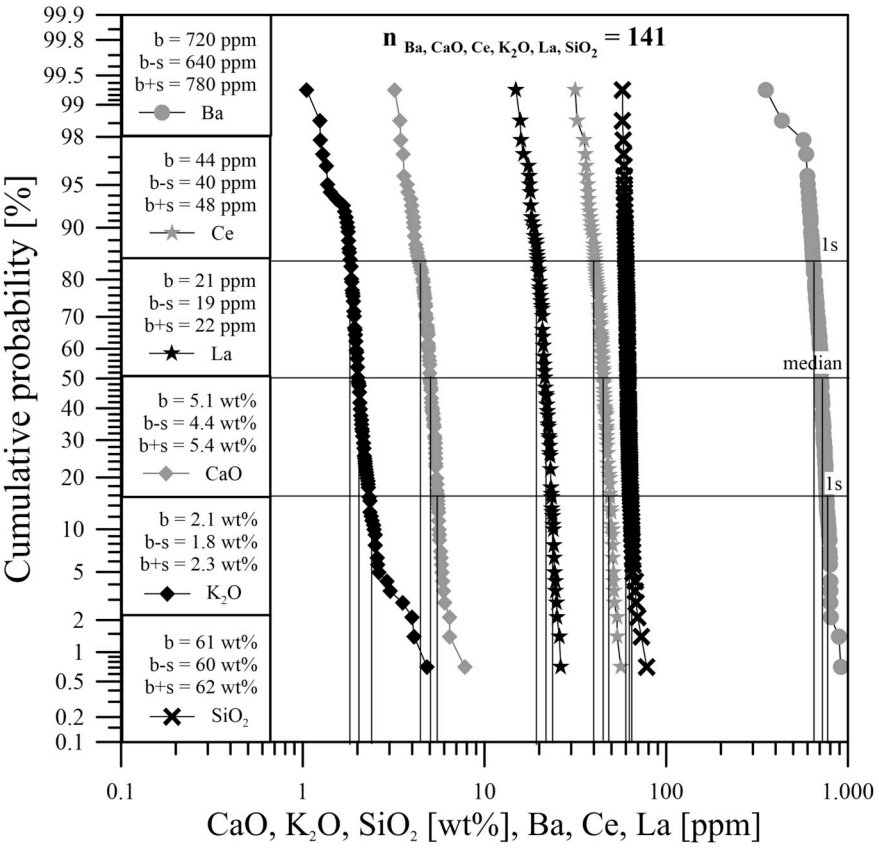


**Fig. 7.** Frequency plots of CaO, $K_2O$, $SiO_2$, Ba, Ce and La all showing unimodal distributions within the range of one standard devation (1s) implying an affiliation of all rocks to the same igneous domain. Neither silicification nor any other advanced alteration style/overprint is displayed revealing not too pronounced alteration styles.

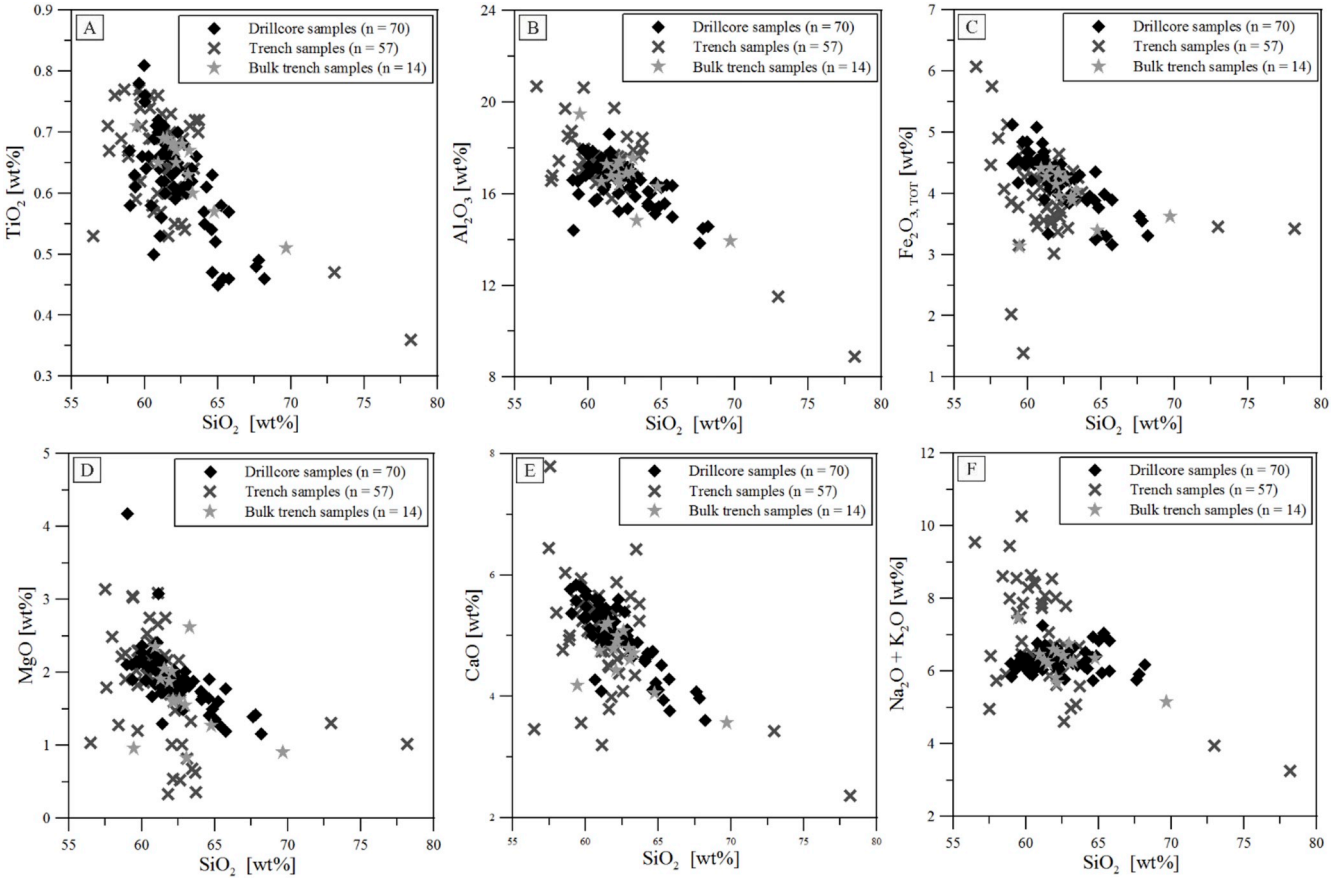


**Fig. 8.** Harker diagrams for Cerro Maricunga samples. Negative linear variation is apparent in drillcore samples for $TiO_2$ (**A**), $Al_2O_3$ (**B**), CaO (**E**) and MgO (**D**), and maybe $Fe_2O_{3,TOT}$ (**C**), reflecting a slight fractionation trend from andesite over rare daciandesite to extremely rare dacite as typical for intermediate volcanic suites. Metasomatic overprint conceals a clear trend for ($Na_2O$ + $K_2O$; **F**).

subduction erosion as suggested by Kay and Mpodozis (2002).

### 4.4.2. Sulfur isotopes

The sulfur isotope composition of some selected samples of barite, gypsum and acanthite (monoclinic $Ag_2S$, stable at temperatures < 173 °C; no argentite, cubic $Ag_2S$, found) is listed in Table 4. Hydrothermal barite, gypsum and acanthite did not precipitate in equilibrium and thus cannot provide relevant information of e.g. the mechanism of ore deposition (Ohmoto and Rye, 1979; Seal II, 2006), but the data (acanthite: $\delta^{34}S$: −0.6 to −0.4; barite/anhydrite: $\delta^{34}S_{sulfate}$: 0.2 to 4.6; Table 5) provide at least indications of the origin of sulfur in the bulk system and the environmental conditions during their formation.

Sulfides with $\delta^{34}S$ values of ± 0‰ are usually interpreted to originate from magmatic fluids; biogenic mediation is invoked if $\delta^{34}S$ values vary more than 10‰ (Ohmoto and Rye, 1979). Typical $\delta^{34}S$ ranges for sulfides in porphyry-Cu deposits are −3 to 1‰ and 8–15‰ for coexisting sulfates, according to Ohmoto and Rye (1979). The Cerro Maricunga data fit well in the igneous sulfide range, but the sulfate values are much lower than for magmatic-hydrothermal sulfide-sulfate pairs.

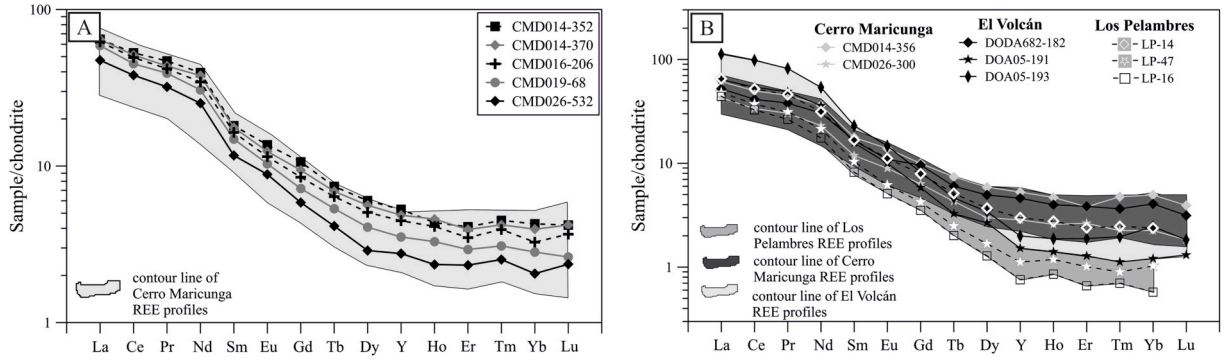


**Fig. 9. A**: Representative chondrite-normalized REE pattern of Cerro Maricunga showing a steep pattern with respect to LREE/HREE fractionation and a relatively flat HREE distribution, indicative of garnet and/or amphibole in the magma source. **B**: Cerro Maricunga REE patterns in comparison to REE patterns of El Volcán and the porphyry deposit of Los Pelambres (Central Chile; database after Schulz, 1997) shown by representative samples. In this context, the general concave-upward curvature of the Cerro Maricunga REE pattern is less pronounced than for El Volcán and Los Pelambres which formed over thick evolved crust. El Volcán rocks are pervasively modified by advanced argillic alteration and silicification maybe causing some analytical problems. The contour lines represent all available analytical data for Cerro Maricunga. Normalization values taken from Taylor and McLennan (1985).

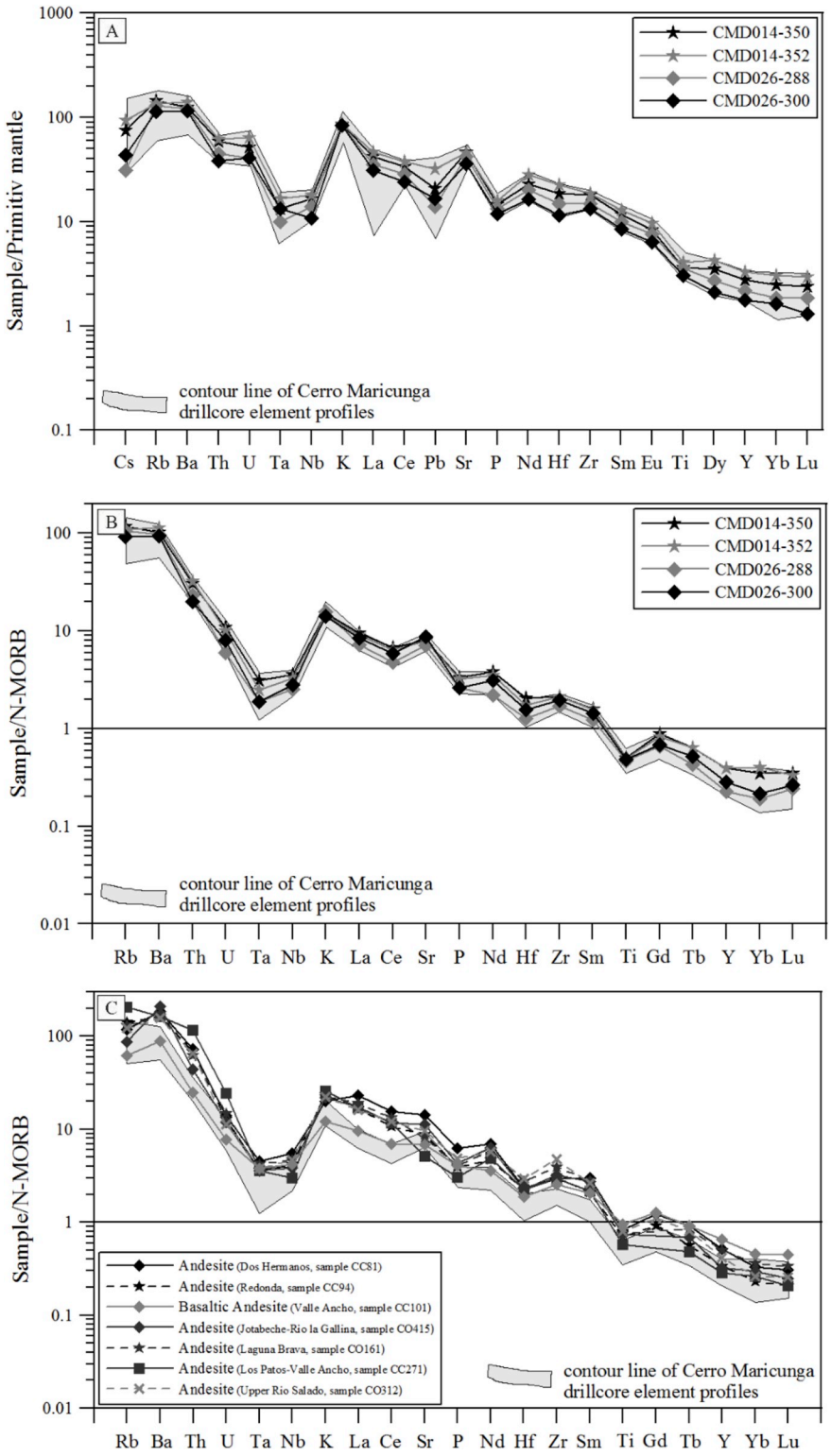


**Fig. 10. A**: Primitive mantle-normalized Spider diagram of representative Cerro Maricunga drillcore samples showing the characteristic enrichment in LIL relative to HFS elements for subduction-related arc magmas, and thus negative anomalies for Nb, P and Ti (normalization values from Lyubetskaya and Korenaga, 2007). The apparent La anomaly arises from samples with pervasive alteration. **B**: N-MORB-normalized Spider diagram for representative Cerro Maricunga drillcore samples with negative anomalies of Ta, Nb, Ti and HREEs indicating an enriched sub-continental lithosphere source (normalization values from Saunders and Tarney, 1984; Sun and McDonough, 1989; Pearce and Parkinson, 1993). **C**: N-MORB normalized Cerro Maricunga samples compared to other Andean adakite-like high-Mg andesite samples from the northern margin of the Chilean-Pampean flat slab (comparative data from Goss and Kay, 2009; Goss et al., 2013; normalization values from Saunders and Tarney, 1984; Sun and McDonough, 1989; Pearce and Parkinson, 1993). The contour lines represent all available analytical data for drillcore samples. (Bulk) trench samples are not considered in order to minimize alteration effects.

The sulfate data exclude biogenic mediation, and the isotope range spans < 7‰ as it should be for sulfate-sulfide pairs of the same deposit (Field and Fifarek, 1985).

Acanthite is the only silver-sulfide species stable at ambient temperature and is generally stable at low hydrothermal temperatures. All silver-bearing species detected during EMP analysis are clearly of supergene origin, including acanthite. Seal II et al. (2000) showed that supergene/weathering processes have only a negligible influence on the sulfur isotope fractionation of sulfides. The acanthite data therefore record the original sulfur source. The $\delta^{34}S$ values of −0.6 to −0.4‰ indicate a magmatic origin of the sulfur, although remobilized by weathering solutions.

In general, transitional porphyry-epithermal silver mineralization in the Maricunga belt is much less important than gold mineralization. Silver mineralization is largely linked to the older mineralization phase lasting from 23 to 21 Ma (La Coipa: 20 Moz Ag; Homepage Kinross, Feb 2019a; (Nueva) Esperanza: 83.2 Moz Ag; Homepage Kingsgate, Feb 2019; Sillitoe et al., 1991) and rarely to the younger one from 13 to

**Table 2**
U-Pb zircon ages by SHRIMP II. Ages are arranged according to the $^{206}Pb/^{238}U$ age column. $^{206}Pb/^{238}U$ ages of the first column have no reliable age information due to too large $^{204}Pb$ correction.

| Spot | $^{206}Pb_c$ | U | Th | $^{232}Th/^{238}U$ | $^{206}Pb^*$ | Age $^{206}Pb/^{238}U$ [a] | Age $^{206}Pb/^{238}U$ [b] | Total $^{238}U/^{206}Pb$ | ± 1σ | Total $^{207}Pb/^{206}Pb$ |
|---|---|---|---|---|---|---|---|---|---|---|
| Unit | % | ppm | ppm | | ppm | | | | | |
| **Neoproterozoic (Ediacaran)** | | | | | | | | | | |
| 1.4a [c] | 0.37 | 396 | 220 | 0.57 | 38.8 | 694 ± 4.5 | 694 ± 4.6 | 8.764 | 0.7 | 0.0654 |
| **Permian (Lopingian)** | | | | | | | | | | |
| 2.3 [d] | 0.61 | 171 | 114 | 0.69 | 6.06 | 258 ± 2.5 | 259 ± 2.4 | 24.3 | 0.9 | 0.0544 |
| 2.7 [d] | 0.27 | 226 | 128 | 0.58 | 7.92 | 257 ± 2.8 | 257 ± 2.9 | 24.54 | 1.1 | 0.0544 |
| 2.4 [d] | 0.48 | 323 | 211 | 0.68 | 11.2 | 254 ± 2.3 | 255 ± 2.2 | 24.77 | 0.9 | 0.053 |
| 1.11a [c] | 1.64 | 89 | 110 | 1.28 | 3.12 | 255 ± 4.6 | 254 ± 4 | 24.39 | 1.6 | 0.0671 |
| **Triassic (Anisian)** | | | | | | | | | | |
| 1.5b [c] | 1.1 | 182 | 226 | 1.28 | 6.16 | 246 ± 2.9 | 247 ± 2.4 | 25.44 | 1 | 0.0565 |
| **Paleogene (Paleocene)** | | | | | | | | | | |
| 3.3 [e] | 1.14 | 447 | 216 | 0.5 | 3.87 | 63.9 ± 0.89 | 64.4 ± 0.82 | 99.2 | 1.2 | 0.0506 |
| 1.9 [c] | 1.47 | 696 | 422 | 0.63 | 5.99 | 63.4 ± 0.83 | 63.9 ± 0.51 | 99.78 | 0.8 | 0.0525 |
| 1.3 [c] | 0 | 713 | 678 | 0.98 | 6.1 | 63.9 ± 0.56 | 63.7 ± 0.57 | 100.5 | 0.9 | 0.0494 |
| 3.2 [e] | 0 | 989 | 497 | 0.52 | 8.42 | 63.6 ± 0.46 | 63.5 ± 0.48 | 100.9 | 0.7 | 0.048 |
| 1.6 [c] | 3.68 | 389 | 225 | 0.6 | 3.31 | 61.2 ± 1.2 | 63.4 ± 0.68 | 101 | 1 | 0.0487 |
| 1.7 [c] | 4.28 | 254 | 78 | 0.32 | 2.14 | 60.2 ± 2.1 | 62.3 ± 0.83 | 102.1 | 1.3 | 0.0539 |
| 1.13b [c] | 4.92 | 323 | 90 | 0.29 | 2.68 | 59.0 ± 2.2 | 61.5 ± 1.1 | 103.6 | 1.7 | 0.0531 |
| 3.4 [e] | 1.99 | 302 | 225 | 0.77 | 2.52 | 61.1 ± 1.3 | 61.3 ± 1.1 | 102.9 | 1.7 | 0.0606 |
| **Paleogene (Oligocene)** | | | | | | | | | | |
| 3.7 [e] | 4.66 | 228 | 7 | 0.03 | 1.01 | 31.7 ± 1.2 | 31.6 ± 0.75 | 193.4 | 2.2 | 0.0851 |
| 3.1 [e] | 3.79 | 238 | 5 | 0.02 | 0.947 | 28.7 ± 0.87 | 28.6 ± 0.62 | 215.9 | 2 | 0.0781 |
| **Neogene (Miocene)** | | | | | | | | | | |
| **I: Early Miocene** | | | | | | | | | | |
| 1.11b [c] | 19.71 | 115 | 9 | 0.08 | 0.407 | 21.5 ± 3.7 | 23.5 ± 0.88 | 242 | 3.3 | 0.14 |
| 1.1 [c] | 2.27 | 395 | 217 | 0.57 | 1.23 | 22.8 ± 0.68 | 22.9 ± 0.54 | 276.2 | 2.2 | 0.06 |
| 3.6 [e] | 12.68 | 124 | 81 | 0.67 | 0.364 | 19.2 ± 1.9 | 20.5 ± 0.81 | 292 | 3.6 | 0.099 |
| 3.8 [e] | 0 | 30 | 25 | 0.87 | 0.093 | 22.9 ± 1.7 | 19.5 ± 1.7 | 281 | 7.3 | 0.163 |
| 3.10 [e] | 21 | 57 | 41 | 0.74 | 0.155 | 16.0 ± 2.6 | 18.6 ± 1 | 317 | 4.9 | 0.113 |
| 1.5a [c] | 0 | 103 | 39 | 0.39 | 0.263 | 19.1 ± 0.71 | 17.5 ± 0.71 | 337 | 3.7 | 0.112 |
| 1.13a [c] | 0 | 271 | 140 | 0.53 | 0.724 | 20.0 ± 0.48 | 17.0 ± 0.54 | 321.3 | 2.4 | 0.167 |
| 1.10 [c] | 56.83 | 216 | 91 | 0.43 | 0.484 | 17.4 ± 4.8 | 16.5 ± 0.44 | 383.8 | 2.6 | 0.06 |
| 1.2 [c] | 10.79 | 387 | 337 | 0.9 | 0.854 | 14.8 ± 0.71 | 16.3 ± 0.36 | 389.3 | 2.1 | 0.0566 |
| 2.1 [d] | 0 | 153 | 95 | 0.64 | 0.342 | 16.8 ± 0.42 | 16.3 ± 0.42 | 384.1 | 2.5 | 0.0704 |
| 1.8 [c] | 36.73 | 111 | 168 | 1.56 | 0.25 | 10.8 ± 3.1 | 16.2 ± 0.6 | 381 | 3.5 | 0.078 |
| 2.2 [d] | 8.57 | 119 | 91 | 0.79 | 0.272 | 15.7 ± 1.2 | 16.2 ± 0.54 | 376 | 3.2 | 0.0886 |
| 1.12 [c] | 14.53 | 204 | 70 | 0.36 | 0.456 | 14.3 ± 1.6 | 16.2 ± 0.44 | 385 | 2.6 | 0.0717 |
| 2.5 [d] | 7.86 | 181 | 115 | 0.66 | 0.399 | 15.2 ± 1.1 | 16.1 ± 0.39 | 389.5 | 2.3 | 0.0667 |
| **II: Middle Miocene** | | | | | | | | | | |
| 2.6 [d] | 7.51 | 159 | 99 | 0.64 | 0.362 | 15.8 ± 1 | 15.9 ± 0.43 | 377.4 | 2.4 | 0.1007 |
| 2.10 [d] | 28.08 | 219 | 155 | 0.73 | 0.48 | 11.8 ± 1.4 | 15.9 ± 0.36 | 391.4 | 2.1 | 0.0732 |
| 2.8 [d] | 12.82 | 166 | 163 | 1.01 | 0.367 | 14.4 ± 1 | 15.8 ± 0.41 | 389.2 | 2.4 | 0.08 |
| 1.4b [c] | 9.01 | 231 | 92 | 0.41 | 0.503 | 14.9 ± 0.85 | 15.8 ± 0.46 | 395 | 2.8 | 0.0704 |
| 2.9 [d] | 16.29 | 75 | 113 | 1.56 | 0.173 | 14.5 ± 1.7 | 15.4 ± 0.61 | 371 | 3.5 | 0.137 |
| 3.5 [e] | 12.95 | 184 | 84 | 0.47 | 0.391 | 13.9 ± 1.5 | 15.3 ± 0.65 | 404 | 4 | 0.076 |
| 3.9 [e] | 0.00 | 234 | 117 | 0.52 | 0.505 | 16.2 ± 0.43 | 14.9 ± 0.46 | 399 | 2.7 | 0.108 |

| Spot | ± 1σ | $^{238}U/^{206}Pb^*$ [a] | ± 1σ | $^{207}Pb^*/^{206}Pb^*$ [a] | ± 1σ | $^{207}Pb^*/^{235}U$ [a] | ± 1σ | $^{206}Pb^*/^{238}U$ (1) | ± 1σ | err corr |
|---|---|---|---|---|---|---|---|---|---|---|
| Unit | | | | | | | | | | |
| **Neoproterozoic (Ediacaran)** | | | | | | | | | | |
| 1.4a [c] | 1.7 | 8.797 | 0.7 | 0.062 | 2.6 | 0.977 | 2.7 | 0.1137 | 0.7 | 0.254 |
| **Permian (Lopingian)** | | | | | | | | | | |
| 2.3 [d] | 2.2 | 24.45 | 10 | 0.05 | 6.2 | 0.279 | 6.3 | 0.0409 | 10 | 0.158 |

**Table 2** (*continued*)

| Spot | ± 1σ | $^{238}U/^{206}Pb^{*}$ [a] | ± 1σ | $^{207}Pb^{*}/^{206}Pb^{*}$ [a] | ± 1σ | $^{207}Pb^{*}/^{235}U$ [a] | ± 1σ | $^{206}Pb^{*}/^{238}U$ (1) | ± 1σ | err corr |
|---|---|---|---|---|---|---|---|---|---|---|
| Unit | | | | | | | | | | |
| 2.7 [d] | 3.1 | 24.61 | 1.1 | 0.052 | 4.4 | 0.293 | 4.5 | 0.0406 | 1.1 | 0.25 |
| 2.4 [d] | 2.5 | 24.89 | 0.9 | 0.049 | 5.5 | 0.272 | 5.5 | 0.0402 | 0.9 | 0.166 |
| 1.11a [c] | 4.2 | 24.8 | 1.8 | | | 0.301 | 15 | 0.0403 | 1.8 | 0.12 |
| **Triassic (Anisian)** | | | | | | | | | | |
| 1.5b [c] | 2.8 | 25.73 | 1.2 | | | 0.255 | 13 | 0.0389 | 1.2 | 0.096 |
| **Paleogene (Paleocene)** | | | | | | | | | | |
| 3.3 [e] | 5.5 | 100.4 | 1.4 | 0.042 | 15 | 0.057 | 15 | 0.01 | 1.4 | 0.096 |
| 1.9 [c] | 2.8 | | | | | | | | | |
| 1.3 [c] | 3.2 | | | | | | | | | |
| 3.2 [e] | 3.4 | 100.9 | 0.7 | 0.048 | 3.4 | 0.066 | 3.5 | 0.0099 | 0.7 | 0.209 |
| 1.6 [c] | 4 | | | | | | | | | |
| 1.7 [c] | 4.7 | | | | | | | | | |
| 1.13b [c] | 5.1 | | | | | | | | | |
| 3.4 [e] | 5.8 | 105 | 2.1 | 0.045 | 24 | 0.059 | 24 | 0.0095 | 2.1 | 0.089 |
| **Paleogene (Oligocene)** | | | | | | | | | | |
| 3.7 [e] | 7.6 | 202.9 | 3.8 | 0.048 | 52 | 0.033 | 52 | 0.0049 | 3.8 | 0.073 |
| 3.1 [e] | 8.3 | 224.4 | 3 | 0.048 | 40 | 0.03 | 40 | 0.0045 | 3 | 0.076 |
| **Neogene (Miocene)** | | | | | | | | | | |
| **I: Early Miocene** | | | | | | | | | | |
| 1.11b [c] | 8.6 | | | | | | | | | |
| 1.1 [c] | 8.5 | | | | | | | | | |
| 3.6 [e] | 12 | 335 | 9.7 | | | | | 0.003 | 9.7 | |
| 3.8 [e] | 19 | 281 | 7.3 | 0.163 | 19 | 0.08 | 21 | 0.0036 | 7.3 | 0.353 |
| 3.10 [e] | 16 | 401 | 16 | | | | | 0.0025 | 16 | |
| 1.5a [c] | 11 | | | | | | | | | |
| 1.13a [c] | 8.4 | | | | | | | | | |
| 1.10 [c] | 10 | | | | | | | | | |
| 1.2 [c] | 7.7 | | | | | | | | | |
| 2.1 [d] | 8.7 | 384.1 | 2.5 | | | | | 0.0026 | 2.5 | |
| 1.8 [c] | 11 | | | | | | | | | |
| 2.2 [d] | 8 | 411 | 7.5 | | | | | 0.0024 | 7.5 | |
| 1.12 [c] | 8.9 | | | | | | | | | |
| 2.5 [d] | 8.6 | 423 | 7.3 | | | | | 0.0024 | 7.3 | |
| **II: Middle Miocene** | | | | | | | | | | |
| 2.6 [d] | 8.7 | 408 | 6.7 | | | | | 0.0025 | 6.7 | |
| 2.10 [d] | 7.3 | 544 | 12 | | | | | 0.0018 | 12 | |
| 2.8 [d] | 8.1 | 446 | 7 | | | | | 0.0022 | 7 | |
| 1.4b [c] | 9.5 | | | | | | | | | |
| 2.9 [d] | 9.3 | 443 | 12 | | | | | 0.0023 | 12 | |
| 3.5 [e] | 13 | 464 | 11 | | | | | 0.0022 | 11 | |
| 3.9 [e] | 10 | 399 | 2.7 | 0.108 | 10 | 0.037 | 11 | 0.0025 | 2.7 | 0.25 |

Errors are 1-sigma; $Pb_c$ and Pb* indicate the common and radiogenic portions, respectively.

[a] Common Pb corrected using measured $^{204}Pb$.

[b] Common Pb corrected by assuming $^{206}Pb/^{238}U$ -$^{207}Pb/^{235}U$ age concordance.

[c] Error in Standard calibration was 0.47% (not included in above errors).

[d] Error in Standard calibration was 0.32% (not included in above errors).

[e] Error in Standard calibration was 0.50% (not included in above errors).

**Table 3**
Sm-Nd isotope data and depleted mantle model ages calculated for selected andesite samples. Model ages were calculated for 10 Ma ($T(DM)_{10}$) and 20 Ma ($T(DM)_{20}$).

| Sample | Sm [ppm] | Nd [ppm] | $^{147}Sm/^{144}Nd$ | ± 2 sigma [%] | $^{143}Nd/^{144}Nd$ | ± 2 sigma | ε | $T(DM)_{10}$ | $T(DM2)_{20}$ |
|---|---|---|---|---|---|---|---|---|---|
| CMD014-350 | 3.917 | 22.12 | 0.10704 | 0.3 | 0.512434 | 0.000002 | −3.9 | 1025 | 1165 |
| CMD014-356 | 4.049 | 22.41 | 0.10918 | 0.3 | 0.512448 | 0.000003 | −3.6 | 1026 | 1143 |
| GM2 | 4.772 | 26.97 | 0.10697 | 0.3 | 0.512449 | 0.000001 | −3.6 | 1003 | 1141 |
| CMD016-216 | 4.086 | 23.42 | 0.10547 | 0.3 | 0.512451 | 0.000002 | −3.5 | 987 | 1138 |
| VS3.2 | 3.308 | 19.42 | 0.10296 | 0.3 | 0.512452 | 0.000002 | −3.5 | 963 | 1136 |
| CMD026-526 | 2.841 | 17.06 | 0.10066 | 0.3 | 0.512458 | 0.000002 | −3.4 | 935 | 1126 |
| CMD019-226 | 3.953 | 22.46 | 0.10637 | 0.3 | 0.512459 | 0.000004 | −3.4 | 984 | 1125 |
| CMD019-68 | 3.715 | 21.80 | 0.10302 | 0.3 | 0.512460 | 0.000006 | −3.4 | 953 | 1123 |
| CMD026-442 | 3.017 | 17.42 | 0.10464 | 0.3 | 0.512467 | 0.000002 | −3.2 | 957 | 1112 |
| CMD026-146 | 3.256 | 18.35 | 0.10725 | 0.3 | 0.512471 | 0.000002 | −3.1 | 975 | 1105 |

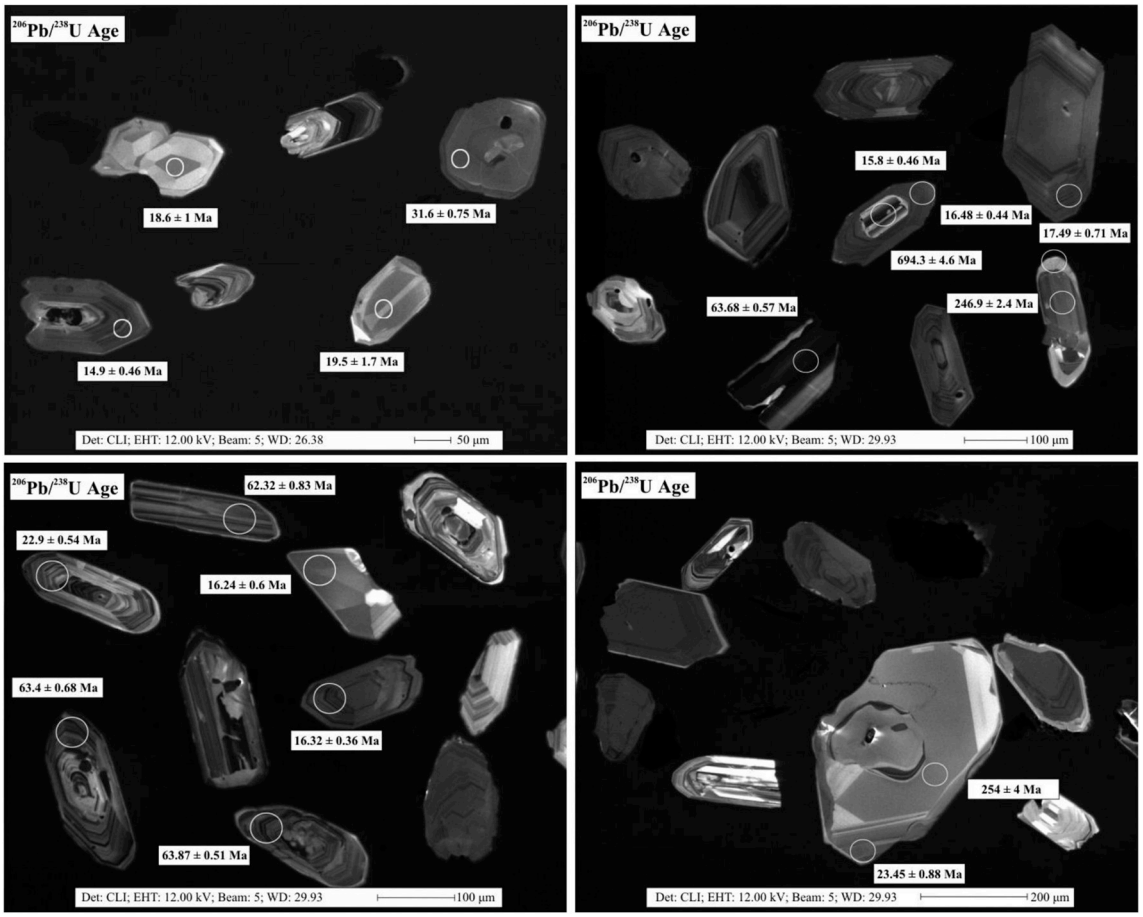


**Fig. 11.** Representative CL images of Cerro Maricunga zircons dated by SHRIMP II. Zircon ages encompass a very broad age spectrum from Neoproterozoic over Permian and Triassic ages to Paleogene (Paleocene, Oligocene) and Neogene (early and mid-Miocene) ages. Some Permian and Paleocene zircon cores have Miocene overgrowth rims. Note that the error is given at 1σ precision.

10 Ma (Aldebarán: 17.3 Moz Ag; Homepage Kinross, Feb 2019b; Sillitoe et al., 1991; Mpodozis et al., 1995).

Considering the broader $\delta^{34}S$ range in the sulfate data, relations are more complex. Firstly, $\delta^{34}S$ values of 0.2‰ for barite can be reconciled with a magmatic origin, but values of up to 4.6‰ are out of the magmatic range. Gypsum values are in the range of 1.5–1.9‰. Notwithstanding their exact formation conditions, sulfates retain mostly their isotope heritage (Seal II et al., 2000). The formation of gypsum after anhydrite is clearly due to supergene alteration, including an increase in volume, but not a change in sulfur isotopy. Moreover, $\delta^{34}S$ values of 1.5–1.9‰ deviate not largely from values unequivocally indicating a magmatic origin. Taking into account the arid environment at the time of formation (compare Alpers and Brimhall, 1988; Evenstar et al., 2005), a superficial evaporitic influence could produce a shift in $\delta^{34}S$ towards more positive values. The same dry conditions could explain the more positive $\delta^{34}S$ barite values.

#### 4.4.3. Oxygen isotopes

The $\delta^{18}O$ values of three barite samples from Cerro Maricunga are quite high at 9.2–13.8‰ (Table 4), and deviate slightly from hypothetical standard magmatic water, with values of 5.5–9.5‰ as summarized in Rollinson (1993) and Seal II et al. (2000). However, the Cerro Maricunga $\delta^{18}O$ data match roughly with magmatic waters of Cornwall (10.8–13.2‰; Sheppard, 1977) and the uncommon magmatic waters shown by Taylor (1974; 2–13‰). Sulfate minerals precipitated in saline lakes, and continental, non-marine, evaporates of Spain and Bolivia have $\delta^{18}O$ values of 11.3–19.7‰ (Seal II et al., 2000, and references therein).

**Table 4**
Sulfur and oxygen isotope data from sulfate and sulfide samples.

| Sample | Mineral | $\delta^{34}S$ [‰] | Mean | 1σ | $\delta^{18}O$ [‰] | 1σ |
|---|---|---|---|---|---|---|
| **Sulfates** | | | | | | |
| CMD014-352 | $BaSO_4$ | 3.0 | 3.0 | 0.04 | | |
| CMD014-352 | $BaSO_4$ | 3.0 | | | | |
| CMD014-394 | $BaSO_4$ | 0.2 | 0.2 | 0.03 | | |
| CMD014-394 | $BaSO_4$ | 0.2 | | | | |
| CMD014-394 | $BaSO_4$ | 1.6 | 1.5 | 0.05 | | |
| CMD014-394 | $BaSO_4$ | 1.5 | | | | |
| CMD016-225 | $BaSO_4$ | 1.3 | | 0.06 | 13.8 | 0.203 |
| T18-4.2M | $BaSO_4$ | 2.5 | | 0.01 | 9.2 | 0.081 |
| CMD014-370 | $BaSO_4$ | 4.6 | | 0.019 | 9.5 | 0.5 |
| CMD014-394 | $CaSO_4 * H_2O$ | 1.9 | 1.7 | 0.23 | | |
| CMD014-394 | $CaSO_4 * H_2O$ | 1.5 | | | | |
| **Sulfides** | | | | | | |
| CMD014-390 | $Ag_2S$ | −0.4 | | 0.01 | | |
| CMD014-356 | $Ag_2S$ | −0.6 | | 0.09 | | |
| CMD016-217 | $Ag_2S$ | −0.6 | | 0.01 | | |

An initial magmatic water source is likely for Cerro Maricunga barite, but the magmatic waters and their precipitates were affected by arid environmental conditions during cooling, provoking a shift to higher $\delta^{18}O$ (compare sulfur isotopes). The formation of barite is late in the evolution of the Cerro Maricunga deposit, so that a climatic change towards more arid conditions implying the involvement of evaporated water is possible during early to mid-Miocene.

## 5. Discussion

### 5.1. Diatreme system

The large-scale diatreme system hosting the low-grade gold mineralization in the Cerro Maricunga area comprises a continuum of magmatic, phreatic and phreatomagmatic breccias as well as pebble dikes and tuffisites. Tectonic and intrusion breccias have not been found.

All breccias are the result of interaction between aqueous fluids, magma and/or solid rock. Considering the overall hydrothermal overprint and the clastic transport of sulfide minerals within tuffisites and pebble dikes, all breccias at Cerro Maricunga are intermineral; a feature which is common for gold-rich porphyry deposits (Sillitoe, 2000). The dimensions of the respective breccia bodies are difficult to delineate. However, phreatomagmatic breccias are by far the most abundant breccia type sharing a large proportion of the rock suite of the Phoenix zone. Magmatic breccias are characterized i.a. by the presence of juvenile fragments as documented in field outcrops and drillcore samples. They are spatially limited and mainly of monomictic nature (Fig. 5). Phreatic breccias, exemplified in particular by single pebble dikes (Fig. 5), are widespread within the remnant volcanic edifice of Ojo de Maricunga; dike swarms are not observed.

According to Sillitoe (2010) pebble dikes are common blind features in porphyry systems, a characteristic that can neither be proved nor rejected for the deeply eroded environment at Cerro Maricunga. They are clearly not post-mineralization, but developed during the waning stages of the hydrothermal system, along with tuffisite dikes (Figs. 5 and 6). Phreatic breccias are formed by steam during flashing when magma approaches cool groundwater (Sillitoe, 1985, 2010). A prerequisite is a self-sealed impermeable cap which vapor can become pressurized. However, the current silicified domains are of very short extent at Cerro Maricunga, arguing against such a process; nonetheless, large-scale silicified caps are known from the adjacent La Coipa mine (Oviedo et al., 1991). Taking into account the removal of some 100 m of rock column of the former Ojo de Maricunga volcano, a formerly much larger extent of silicified paleo-cap rocks is possible. This setting would explain a former close connection or more likely telescoping of a residual quite shallow, porphyry-type system and the now removed near-surface epithermal system, and is in agreement with Sillitoe's (2010) argumentation for pebble dikes as downward transition to porphyry intrusions. Andesitic dikes range from few cm to some dm in thickness in outcrop and attain < 5 m in drillcore (Fig. 5). Similar to the El Salvador site (Gustafson and Hunt, 1975), the dikes transect pebble dikes and are linked to phreatic activity.

Phreatomagmatic breccias share the largest proportion of clastic mineralized rocks at Cerro Maricunga. These polymict, matrix-supported breccias crop out over large distances in trenches and are abundant in drillcore (Fig. 6). Interaction of cool groundwater with magma is documented by a wealth of juvenile clasts. Sillitoe (1985) ranked phreatomagmatic breccias among late events in gold-rich porphyries, a circumstance not applicable to Cerro Maricunga due to crosscutting mineralized quartz veinlets and contained veinlet clasts (Fig. 6). Combined with single and polyclastic (daci)andesitic and dacitic clasts, these fragments give the clearest evidence for multiple-stage, syn-mineral brecciation within this area. The diatreme system, comprising large parts of the Phoenix zone, was not only formed by phreatomagmatic activity, but rather by a combination of phreatomagmatic, magmatic and phreatic events, as envisaged by Lorenz (2003) and Sillitoe (2010). Diatremes can reach depths of > 2.5 km (Lorenz, 2003). The Cerro Maricunga diatreme has a proven depth of > 1500 m below the current summit at 4978 m, as proven by inclined drilling at the flank of the volcano. The total dimensions currently cannot be outlined.

Apart from breccias, ignimbrites were deposited. Concurrently, andesitic and rarely daciandesitic flows were released by the Ojo de Maricunga volcano. Andesitic dikes truncate shallow porphyritic intrusions and volcanic ejecta. All these different rock types contributed to varying degree to the formation of a complex, large-scale diatreme system hosting the syngenetic gold mineralization.

### 5.2. Origin of phenocrysts and calculated temperatures of mineral phases

Plagioclase crystals in the Cerro Maricunga rocks reveal a distinct polysynthetic twinning with both oscillatory and reverse zoning. These patterns suggest open-system processes with shifting Ca/Na ratios in the parent melt, e.g. due to replenishment by new magma batches or evacuation during eruption events leading to changes in P-T conditions and water saturation in the melt.

Using the two two-feldspar thermometers of Putirka (2008) temperatures between about 800° ± 44 °C (at 1 kbar; 816° ± 30 °C) and 885° ± 44 °C (at 13 kbar; 898° ± 13 °C) result for both large phenocrysts and small lath-shaped crystals within igneous groundmass (ESM part C). All data fulfill the test of validation for Ab-An exchange. Considering only plagioclase, Putirka (2005, 2008) recommended a plagioclase-liquid thermometer useable at low temperatures and in hydrous systems. The best temperature match between the two-feldspar thermometers and the plagioclase-liquid thermometer is by a water content of 7 wt% (temperature interval of 875–916° ± 48 °C). However, the water content is considered as slightly too high, and 6 wt% water for wet melts may be more realistic (Richards, 2011; Richards et al., 2012). Using the hygrometer of Lange et al. (2009) the same combination of relatively low formation temperatures, but quite high primary water contents, irrespective of the applied pressure, results. These results fit well with for example the findings of Annen et al. (2006) that $H_2O$-rich andesitic melts are produced at temperatures of 850°–1050 °C.

Quartz eyes are frequently observed within the magmatic suite of porphyry systems, as exemplified by the El Indio (Jannas et al., 1990) and the Bajo de la Alumbrera deposits (Harris et al., 2003, 2004), however, their origin is still controversially discussed. They may be ranked as porphyroblasts (i.a. Hopwood, 1976) or phenocrysts (i.a. Vernon, 1986, 1987; Watt et al., 1997; Bineli Betsi and Lentz, 2010), and rarely are seen as fragments of early veins or quartz-rich bodies (Williams and Carmichael, 1987). Watt et al. (1997) traced the rounded nature of quartz grains at Esperanza to dissolution or melting during

**Table 5**
Temperature results for Cerro Maricunga quartz eyes obtained by the revised TitaniQ geothermometer after Thomas et al. (2010), applying a $TiO_2$ activity of 0.81. The titanium concentration was analyzed by EMPA and by LA-ICP-MS.

| Quartz-eye | Depth | | | | | | | | | | | | | | | | | | | | | | | |
|---|---|---|---|---|---|---|---|---|---|---|---|---|---|---|---|---|---|---|---|---|---|---|---|---|
| | 50 km | | | 40 km | | | 30 km | | | 25 km | | | 20 km | | | 10 km | | | 8 km | | | 2 km | | |
| | mean | min | max | mean | min | max | mean | min | max | mean | min | max | mean | min | max | mean | min | max | mean | min | max | mean | min | max |
| $1_{core}$ | 711 | 691 | 730 | 658 | 639 | 676 | 603 | 586 | 621 | 576 | 560 | 593 | 549 | 533 | 566 | 495 | 480 | 510 | 484 | 470 | 499 | 452 | 438 | 466 |
| $1_{fringe}$ | 793 | 782 | 804 | 735 | 725 | 746 | 677 | 667 | 687 | 648 | 638 | 657 | 618 | 609 | 628 | 560 | 551 | 568 | 548 | 539 | 557 | 513 | 504 | 521 |
| $2_{core}$ | 773 | 771 | 775 | 717 | 715 | 719 | 659 | 657 | 661 | 630 | 629 | 632 | 602 | 600 | 604 | 544 | 543 | 546 | 533 | 531 | 534 | 498 | 497 | 500 |
| $2_{fringe}$ | 1067 | 1035 | 1098 | 994 | 964 | 1024 | 921 | 892 | 949 | 884 | 856 | 911 | 847 | 820 | 874 | 773 | 748 | 798 | 759 | 734 | 783 | 714 | 691 | 738 |
| 3 | 731 | 673 | 767 | 677 | 622 | 710 | 622 | 570 | 653 | 594 | 544 | 625 | 567 | 518 | 596 | 512 | 466 | 539 | 501 | 456 | 528 | 467 | 424 | 493 |
| 4 | 733 | 703 | 775 | 679 | 650 | 719 | 670 | 597 | 612 | 641 | 632 | 585 | 612 | 543 | 604 | 553 | 489 | 546 | 542 | 479 | 534 | 507 | 447 | 500 |
| 5 | 785 | 747 | 811 | 728 | 692 | 753 | 670 | 636 | 693 | 641 | 608 | 663 | 612 | 580 | 633 | 553 | 524 | 574 | 542 | 512 | 562 | 507 | 479 | 526 |
| 6 | 775 | 624 | 917 | 719 | 575 | 852 | 661 | 526 | 787 | 632 | 501 | 754 | 604 | 477 | 722 | 546 | 427 | 656 | 534 | 418 | 643 | 500 | 388 | 604 |
| 7 | 717 | 471 | 837 | 663 | 431 | 777 | 609 | 390 | 716 | 582 | 370 | 686 | 555 | 349 | 655 | 500 | 308 | 594 | 489 | 300 | 582 | 457 | 276 | 545 |
| 8 | 738 | 537 | 859 | 683 | 493 | 798 | 628 | 449 | 736 | 600 | 426 | 705 | 572 | 404 | 674 | 517 | 360 | 611 | 506 | 351 | 599 | 472 | 324 | 562 |
| 9 | 719 | 471 | 853 | 666 | 431 | 792 | 611 | 390 | 730 | 584 | 370 | 699 | 557 | 349 | 668 | 502 | 308 | 606 | 491 | 300 | 594 | 459 | 276 | 557 |
| 10 | 761 | 631 | 862 | 706 | 582 | 800 | 649 | 533 | 738 | 620 | 508 | 707 | 592 | 483 | 676 | 535 | 433 | 613 | 524 | 423 | 601 | 490 | 394 | 563 |
| 11 | 681 | 556 | 827 | 629 | 511 | 767 | 577 | 449 | 707 | 551 | 426 | 677 | 524 | 404 | 647 | 472 | 360 | 586 | 462 | 351 | 574 | 430 | 324 | 538 |
| 12 | 766 | 606 | 858 | 710 | 559 | 797 | 653 | 510 | 735 | 625 | 605 | 704 | 596 | 462 | 673 | 539 | 414 | 610 | 527 | 404 | 598 | 493 | 375 | 561 |
| 13 | 707 | 556 | 814 | 654 | 511 | 756 | 600 | 466 | 696 | 573 | 443 | 666 | 546 | 420 | 636 | 493 | 375 | 576 | 482 | 366 | 564 | 449 | 338 | 528 |
| 14 | 691 | 572 | 814 | 639 | 526 | 756 | 586 | 480 | 696 | 560 | 456 | 666 | 533 | 433 | 636 | 486 | 387 | 576 | 470 | 377 | 564 | 438 | 350 | 528 |
| 15 | 721 | 511 | 813 | 667 | 469 | 754 | 613 | 426 | 694 | 585 | 404 | 665 | 558 | 383 | 635 | 503 | 340 | 575 | 492 | 331 | 563 | 460 | 305 | 527 |
| 16 | 708 | 511 | 842 | 655 | 469 | 782 | 601 | 426 | 721 | 574 | 404 | 690 | 547 | 383 | 660 | 493 | 340 | 598 | 483 | 331 | 586 | 450 | 305 | 549 |
| $17_{LA\text{-}ICP\text{-}MS}$ | 753 | 739 | 778 | 697 | 684 | 721 | 641 | 629 | 663 | 613 | 601 | 635 | 585 | 573 | 606 | 528 | 518 | 548 | 517 | 506 | 536 | 483 | 473 | 502 |
| mean (without fringes) | 734 | | | 679 | | | 627 | | | | 599 | | | | 571 | | | | 505 | | | 471 | | |
| mean (fringes) | 930 | | | 865 | | | 799 | | | | 766 | | | | 733 | | | | 654 | | | 614 | | |

Footnote: The main critical issue of Ti-in-quartz geothermometry is the correct estimation of the activity of $TiO_2$. During microscopy work, no rutile was observed, but large quantities of late-magmatic Fe-Ti oxides and some titanite laths included in feldspar. For a similar setting, Wark and Watson (2006) stated a $TiO_2$ activity of $\geq 0.5$ as reasonable, and Hayden and Watson (2007) denoted a $TiO_2$ activity of mostly $\geq 0.6$ at typical magmatic temperatures. We calculated $a_{TiO2}$ by coexisting Fe-Ti oxides after the method of Ghiorso and Gualda (2013) obtaining values between 0.61 and 0.92 with an average of 0.81. Despite some criticism of i.a. Thomas and Watson (2012) regarding the usage of Fe-Ti oxide temperature, the values seem reasonable with respect to an andesitic magma with large amounts of magnetite-ilmenite pairs.

thermal or thermal-chemical disequilibrium within melt and interpreted the embayments as result of convective dissolution triggered by gas bubbles. Open-system processes are envisaged by Streck (2008). Vasyukova et al. (2010) argued for a concomitant magmatic and hydrothermal origin by reason of an in situ crystallization of quartz eyes instead of crystallization in a magma chamber or during magma ascent and convection.

At Bajo de la Alumbrera, Harris et al. (2003, 2004) distinguished rounded and irregular, partly embayed and apparently resorbed individual quartz eyes from those composed of elliptical, small crystals consisting of sugary aggregates. The latter are interpreted to have been formed from an exsolving magmatic aqueous fluid at the earliest stage of separation from a silicic magma. Based on the visual quartz-eye description, there is a clear match between Bajo de la Alumbrera and Cerro Maricunga quartz eyes. Nonetheless, the interpretation of quartz eyes as result of resorption processes seems most likely.

Some Cerro Maricunga quartz eyes have overgrowths of non-hydrothermal origin surrounding well-rounded quartz-eye cores that were exposed previously to dissolution. Consequently, after a first dissolution phase a growth stage succeeded. It cannot be proved if this second growth stage took place within a magma chamber or during cooling at the emplacement site, but individual quartz eyes within the Cerro Maricunga domain are clearly of magmatic and not of hydrothermal origin. They were formed during open-system processes and are seen as phenocrysts with local hydrothermal overgrowth.

The Ti-in-quartz geothermometer (Wark and Watson, 2006; Thomas et al., 2010) can be used for thermometry. The Ti content of quartz eyes was measured by LA-ICP-MS and displayed a quite homogeneous distribution within one and the same crystal (Fig. 12). Considering a formation depth in the middle crust (~25 km), an average formation temperature of ~600 °C is obtained (temperature range: ~550° to 640 °C). For a formation depth of 30–40 km in a flat-slab setting, slightly higher temperatures of ~630 °C or ~680 °C are calculated (Table 5). Applying a formation depth of 8–10 km gives average formation temperatures of ~505°–~515 °C. However, the formation of quartz eyes within a shallow magma chamber is unrealistic, because the quartz crystals formed in a silicate melt, not in a sub-solidus situation. In this context, the formation of quartz-eye cores at a middle to lower crustal level (~500°–600 °C) during the transport from a deep hot zone or a MASH zone to a medium-shallow magma chamber is realistic, the position where the quartz eyes became corroded. The calculated temperatures for quartz fringes are throughout higher than those of quartz cores and can be explained by contamination due to Ti-bearing microcrystals.

The small anhedral shape of secondary apatite is indicative of apatite growing in the presence of a liquid or vapor, in comparison to elongated to acicular shapes of primary magmatic apatite delineating a growth at large degree of supersaturation (Piccoli and Candela, 2002). Igneous apatite associated with felsic-intermediate rocks has a restricted range in composition with 50–100% F, 0–50% OH and < 20% Cl in F-Cl-OH space (Piccoli and Candela, 2002), as reflected by the fluorapatite composition. The post-magmatic chlorapatite attests to chlorine in the hydrothermal fluid system.

### 5.3. Adakite-like magmatism

Adakites and adakite-like rocks are widely discussed in the literature with respect to volcanic-arc rocks (i.a. Kay, 1978; Defant and Drummond, 1990; Defant et al., 1991; Stern and Kilian, 1996; Prouteau et al., 2001) and porphyry systems (i.a. Richards and Kerrich, 2007; Richards, 2011; Richards et al., 2012). Originating from an uncommon Aleutian Mg-andesite (Kay, 1978) the “label” adakite was inserted first into the petrologic and later also in the economic geology literature (i.a. Richards and Kerrich, 2007; Richards, 2009, 2011; Richards et al., 2012). The defining criteria comprise $SiO_2$ ≥56 wt%, $Al_2O_2$ ≥ 15 wt%, MgO < 3 wt%, #Mg ~0.5, Sr > 400 ppm, low Y and HREE (Y ≤ 18 ppm, Yb ≤ 1.9 ppm), low HFSEs, Ni ≥ 20 ppm, high Sr/Y and La/Yb ratios and are easy to adopt to any rock type without considering its geologic setting in detail. In doing so, Cerro Maricunga andesites are identified as very close to adakites, using the differentiation criteria after Richards and Kerrich (2007; Fig. 13). Furthermore, they retrace clear differentiation trends for garnet, amphibole, clinopyroxene, titanite and zircon in contrast to common plagioclase trends of the andesite-dacite-rhyolite series, and therefore fulfill additional criteria after Defant and Drummond (1993) and Castillo et al. (1999; Fig. 14).

The igneous rocks at Cerro Maricunga have a geochemical signature that characterizes them as close to adakites, but their REE signature points moreover to a source with garnet and/or amphibole residuum. Such a source could be the lower continental crust as indicated by homogeneous $\varepsilon_{Nd}$ values between −3.1 and −3.9 for 10 Ma, and −3.0 to −3.8 for 20 Ma (Table 3; Fig. 15). The depleted mantle model age is ~1 Ga suggesting a Proterozoic basement (Table 3). The basement material can either directly originate from Precambrian terranes (Ramos et al., 2010) forming the deep crust below the Ojo de Maricunga volcano or be entrained partially by forearc subduction erosion (Kay and Mpodozis, 2002) with subsequent recycling into the mantle and uptake into Cerro Maricunga magmas. Although, Cerro Maricunga magmas have a conspicuous similarity with Pircas Negras and Dos Hermanos lavas (Goss et al., 2013) showing likewise adakitic signatures, they differ by lower Ni and Cr values. Whereas Dos Hermanos andesites result from partial melting of eclogitic crust linked to ponded mantle-derived arc magmas, Pircas Negras andesites contain partial melt components entrained during mafic fore-arc subduction erosion that reacted with the overlying mantle wedge (Goss et al., 2013). However, these magmas evolved when crustal thickness was > 60 km (Goss et al., 2013).

The Cerro Maricunga REE signature reflects a magma source in the deep crust or at the crust-mantle transition at depths ≥45 km, where the magma was in equilibrium with a garnet- and amphibole-bearing residue due to crustal thickening within the Chilean flat slab setting. The Cerro Maricunga igneous rocks fit well in the overall situation in late Oligocene to mid-Miocene with calc-alkaline to mildly tholeiitic continental volcanic rocks in the flat slab region (Kay et al., 1991), with quite similar trace element patterns within other domains at the southernmost extremity of the CVZ (Walker et al., 1991). Kay et al. (1991) suggested a MASH-like zone with mantle-derived basalts contaminated by lower crust as most likely source region for the magmas in the northern Chilean flat slab segment, but they discussed also

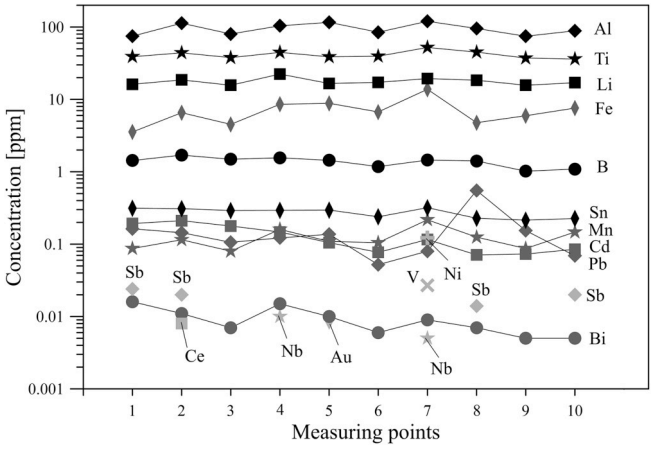


**Fig. 12.** Trace element abundance within an individual quartz eye (LA-ICP-MS analysis) reflecting quite homogeneous element distributions for Al, B and Ti, whereas Bi, Cd, Fe, Mn and Pb display some scatter. Single values close to the detection limit could be obtained for Au, Cr, Nb, Ni, Sb and V. The conspicuous Pb spike of measuring point eight is probably an artefact from sample preparation.

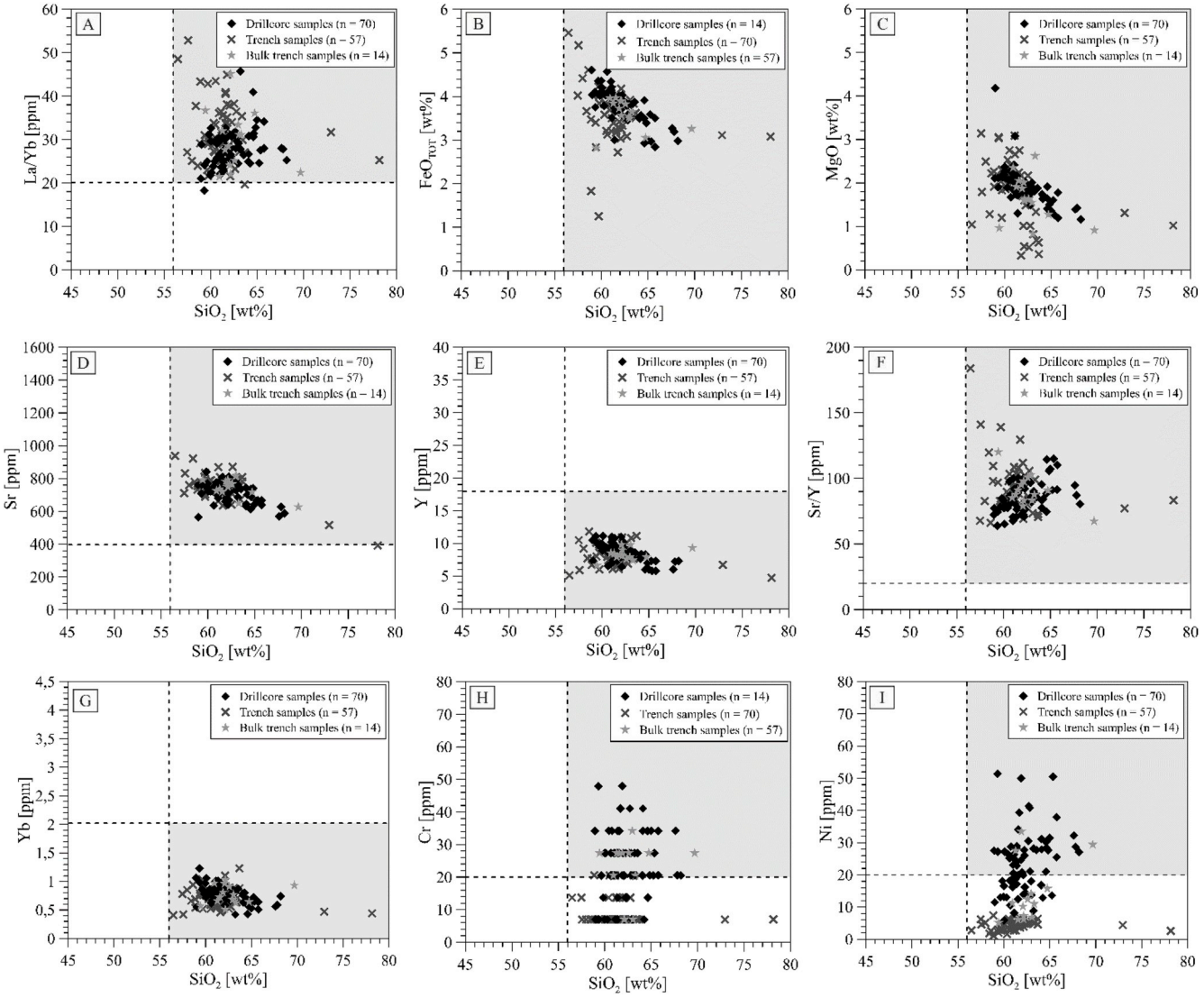


**Fig. 13.** Variability plots after Richards and Kerrich (2007) used for identification of adakites (grey field) applied to Cerro Maricunga rocks, identifying these as close to adakites. All samples plotting in white fields have no adakite affiliation.

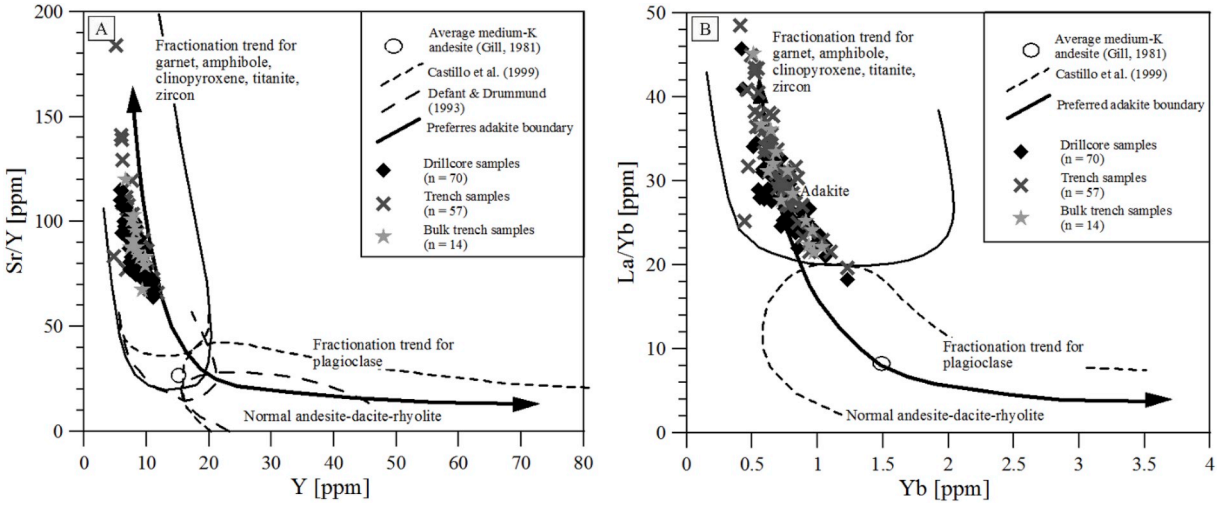


**Fig. 14.** Plots of Sr/Y vs Y (after Defant and Drummond, 1993) and La/Yb vs Yb (after Castillo et al., 1999) used for differentiation between adakites and common rocks of the andesite-dacite-rhyolite series. The typical fractionation trends for plagioclase and for the assemblage of garnet, amphibole, clinopyroxene, titanite and zircon are shown schematically. Cerro Maricunga rocks plot close to adakites.

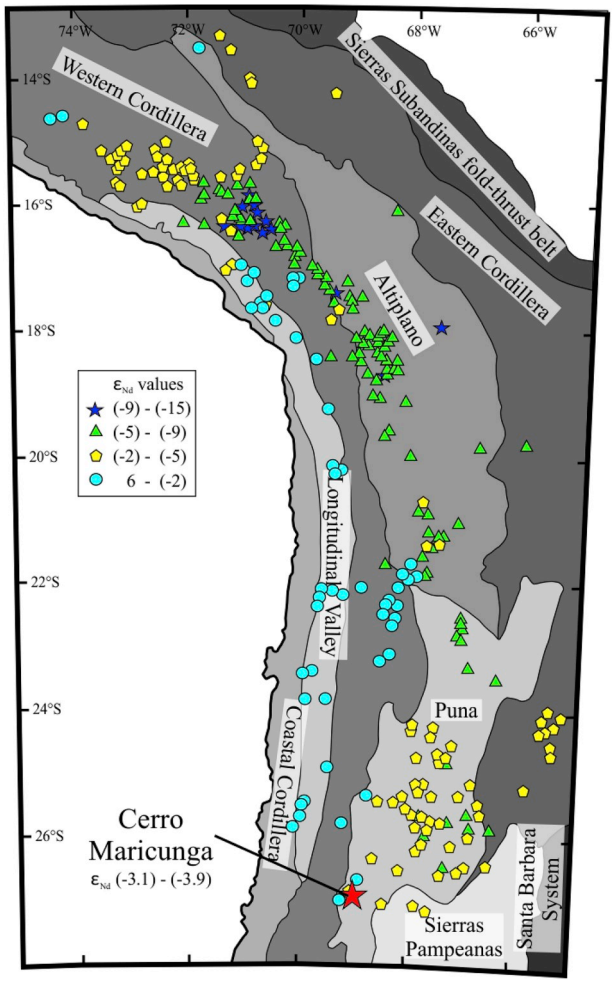


**Fig. 15.** Overview map of present-day $\varepsilon_{Nd}$ data of the Central Andes and Cerro Maricunga (modified after Mamani et al., 2008).

alternative mechanisms for magma generation including partial melting of lower crust. Regardless of the melt processes, a garnet- and ± amphibole-bearing granulite residue is firmly established.

Thus, there is no need to postulate a slab-derived component, product of partial melting of an oxidized slab, which could contribute to magma generation at the Ojo de Maricunga volcano. Instead, a similar evolution as shown for many Cretaceous to Pliocene porphyry-copper deposits in the Chilean Andes and worldwide (compare Richards, 2011, and Richards et al., 2012) is envisaged. The main difference is the evolution in a flat slab setting where a high water fugacity is inherent in the upper mantle or lower crust and amphibole-dominated and plagioclase-suppressed fractionation is typical. In this context, the evolution of Cerro Maricunga is somewhat special, but does not deviate largely from the formation of the gold porphyries close-by, albeit there is a time gap of 5–7 Ma. Richards et al. (2012) postulated an absent or at least suppressed volcanic activity during the formation of fertile porphyry deposits, a linkage that does not apply for Cerro Maricunga. However, preceding long-lasting non-fertile magmatic activity, another characteristic of porphyry systems is traceable by means of zircon age data (Richards et al., 2012).

Some Chilean porphyry deposits, like the giants in central Chile, do not reveal these special garnet-controlled REE patterns, and likewise do not show temporal related changes in geochemistry, albeit they were formed within a thick sequence of Cretaceous to Pliocene rocks (Hollings et al., 2005). The impact of the subducting Juan Fernandez ridge in that region is still uncertain (i.a. Kay and Mpodozis, 2002; Hollings et al., 2005). Apart from this, the giants possess likewise the characteristic trace element signatures of a subarc mantle source.

The previous establishment of a stable MASH zone during a prolonged magmatic arc evolution is seen as a prerequisite for the formation of fertile porphyry-related magmas (Richards et al., 2012), and is envisaged for the Maricunga belt by Kay et al. (1999). Late magmas are in general geochemically more evolved and consequently more hydrous, crucial for the emplacement of arc magmas in shallow crustal levels with concomitant magmatic-hydrothermal activity. As shown by Kay and Kay (2002), simple crustal thickening or subduction erosion are sufficient for the formation of Andean adakites. The igneous rocks at Cerro Maricunga evolved within a mature arc with thickened crust explaining the adakite-like signatures.

### 5.4. Magmatic-geochemical and temporal setting of Cerro Maricunga

All $^{206}Pb/^{238}U$ zircon ages are interpreted as magmatic ages implying a large population of inherited zircons from the basement. One zircon has an unexpectedly old Neoproterozoic age, previously not observed in rocks from the Maricunga belt. However, outcrops of Precambrian rocks are known from other areas further north, and among others, Kay and Abbruzzi (1996) speculated on a significant involvement of old basement in Andean magmatism. Moreover, Kay et al. (1999) showed that flat slab magmas possess geochemical fingerprints implying assimilated crustal components of old basement. And Kay et al. (2014) gave a detailed image of magma modification within the Maricunga belt and surrounding areas by contamination of mantle-derived magmas by lithospheric components by fore-arc subduction erosion and delamination in a varyiably thickening crust over the last ~25 Ma. All in all, a magma source region within the lower crust, reflected by inherited zircons as restite components, can easily be adopted for Cerro Maricunga rocks, and is in addition confirmed by Nd isotope data.

Paleozoic rocks crop out in small domains north and southwest of Cerro Maricunga, as well as south of Pantanillo (Fig. 2). Outcrops of Mesozoic rocks are at short distance north and west of Cerro Maricunga and within a long strip in the western part of the belt. Both, Paleozoic and Mesozoic rocks are supposed to form the direct underlying basement of Cenozoic rocks within the belt. The existence of several Paleozoic terranes with Mesoproterozoic Grenville-age continental basement at the southern end of the CZV was suggested by e.g. Ramos et al. (2010), with the Chilenia terrane at the area of the Ojo de Maricunga volcano.

Hence, the occurrence of zircons of Permian and Triassic age is by assimilation of country rocks of corresponding age during Cenozoic magma ascent, as the reworking of older arc rocks is common (e.g., Kay et al., 2014). Oligocene rocks are not widespread within the belt and occur mainly as small outcrops in the periphery of younger Cenozoic igneous rocks. The surroundings of Ojo de Maricunga are mapped as volcanic and intrusive rocks of early to mid-Miocene age, a setting well reflected by the dated zircons.

Gold mineralization at Cerro Maricunga is dated at 17.9 ± 0.25 Ma by Re-Os on molybdenite (Lohmeier, 2017); the lifespan of hydrothermal systems in the Maricunga belt setting is likely some 100,000 years (Muntean and Einaudi, 2001). Therefore, the 18.6 ± 2.0 Ma zircon age could represent the age of emplacement of the ore-related porphyry/diatreme event at Ojo de Maricunga. All older Miocene zircon ages are seen as pre-mineralization, and all younger ages as post-mineralization magmatic pulses. The youngest zircon age of 14.9 ± 0.5 Ma characterizes the final magmatic activity at Ojo de Maricunga within the area of Cerro Maricunga.

The available K-Ar and Ar-Ar age data for bulk rock of the Ojo de Maricunga volcanic center are between 14.1 ± 0.6 Ma and 15.8 ± 0.9 Ma (Cornejo et al., 1993; McKee et al., 1994; Kay et al., 1994b; Mpodozis et al., 1995) and mark all post-mineralization events. They match well with the new zircon ages, in particular as the 15.8 ± 0.8 Ma K-Ar age of Cornejo et al. (1993) represents the

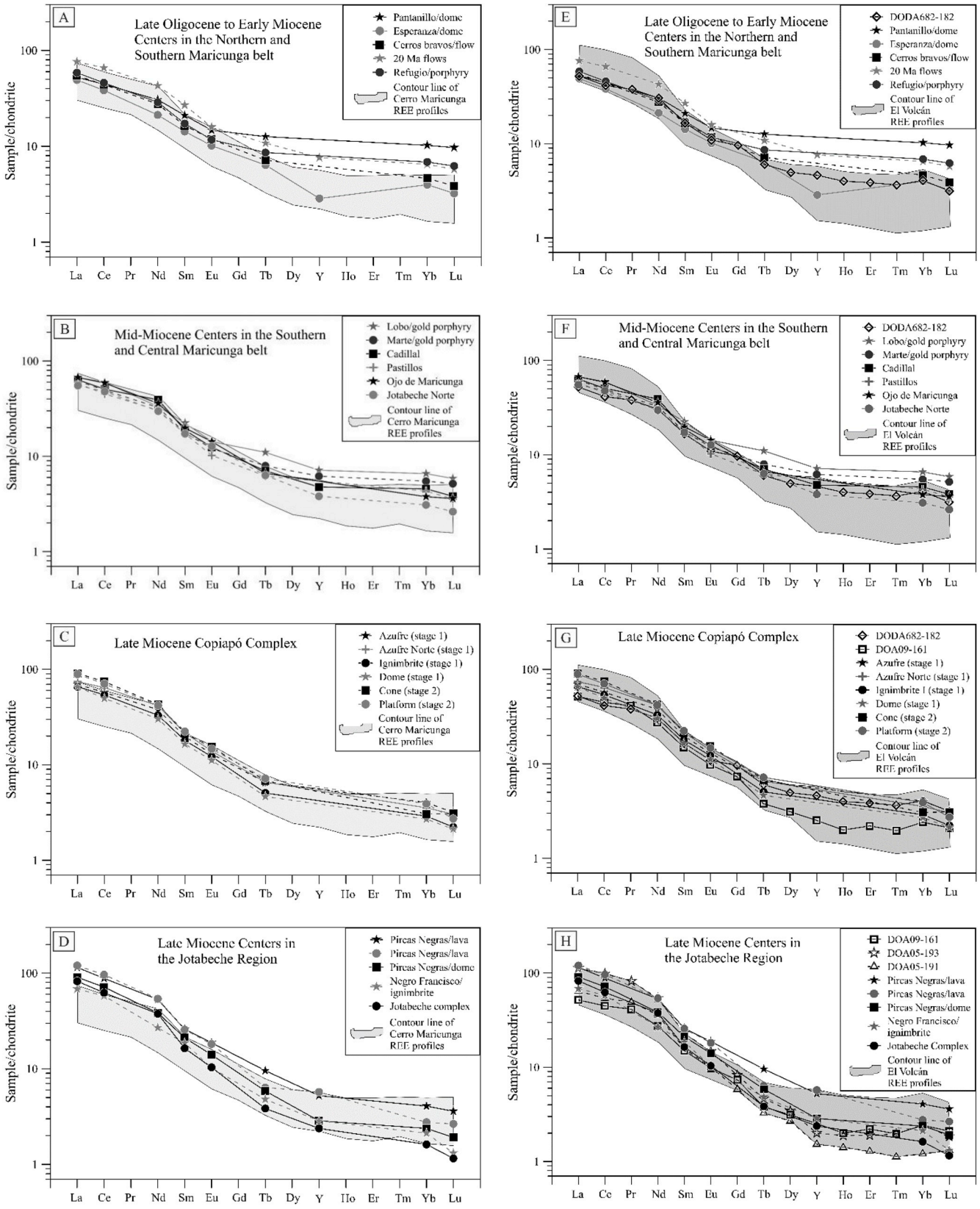


**Fig. 16.** Cerro Maricunga (**A–D**) and El Volcán (**E–H**) igneous rocks shown in the context of temporal and geochemical evolution during the last ~25 Ma within the Maricunga belt, modified after Kay et al. (1999). **Cerro Maricunga**: The best match between Cerro Maricunga REE patterns and REE patterns representative for regional magmatic rocks of the belt is for late Miocene, formed over a thick continental crust (≥45 km) suggesting that the crustal thickening in the central part of the Maricunga belt, in the surroundings of Ojo de Maricunga, was more advanced in early and mid-Miocene than previously assumed. **El Volcan**: In contrast to the Cerro Maricunga igneous rocks, El Volcán reference samples show a more diversified REE pattern leading to matches of single samples with Maricunga belt REE patterns for late Oligocene to late Miocene, due to the multiple-stage history of Volcán Copiapó hosting the El Volcán domain.

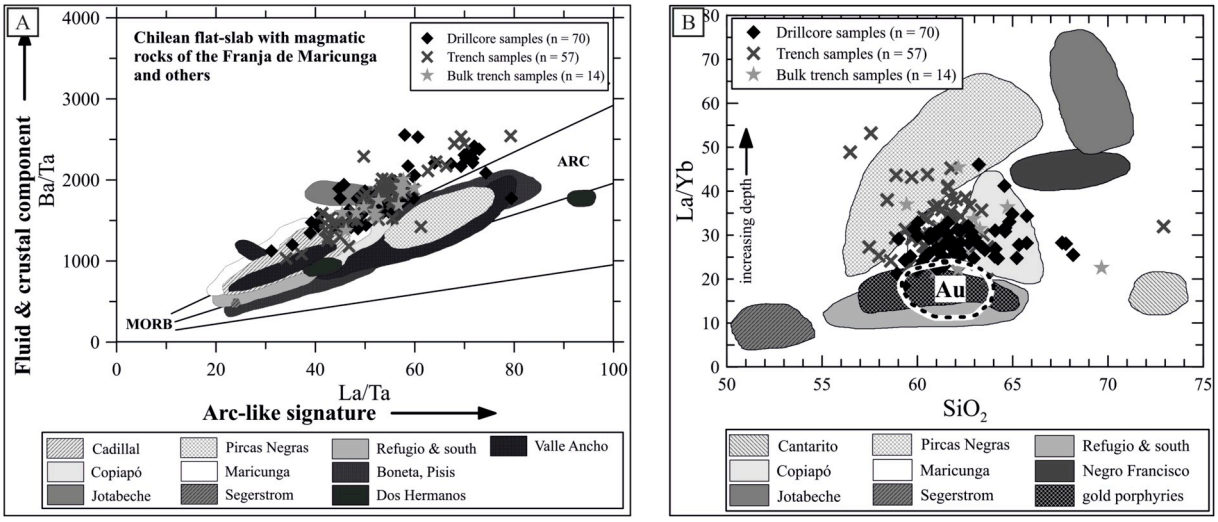


**Fig. 17. A**: Cerro Maricunga igneous rocks displayed in the La/Ta vs Ba/Ta diagram modified after Kay and Mpodozis (2002) showing the involvement of both mantle-derived fluids and crustal material during the evolution of igneous rocks in the Maricunga belt as well as for Cerro Maricunga. **B**: Cerro Maricunga igneous rocks displayed in the $SiO_2$ vs La/Yb diagram modified after Kay et al. (1999). The Cerro Maricunga prospect is not within the gold porphyry reference field (comprising i.a. Lobo-Marte) due to less fractionated magmatic rocks at the gold porphyry reference sites.

hydrothermal altered late central dome. In addition, few K-Ar ages for biotite of 13.7 ± 2.6 Ma (Quirt, 1972) and 14.3 ± 1.6 Ma (Zentilli, 1974) of tuffs/ignimbrites and few K-Ar ages for hornblende of pyroclastic rocks of 16.1 ± 0.6 Ma and 16.1 ± 0.8 Ma (recalculated from Zentilli, 1974; Kay et al., 1994b) and 15.1 ± 0.7 (Mpodozis et al., 1994) are available. Whereas the ~16 to 15 Ma ages fit well in the time frame, the younger ages point to a longer lasting post-hydrothermal magmatic explosive activity within the area of the Ojo de Maricunga complex as implied by the new zircon ages.

Age data of centers to the south of the Ojo de Maricunga center including the Santa Rosa (15.4 ± 0.55 Ma, McKee et al., 1994; 13.8 Ma, González-Ferrán et al., 1985), Cerro Lagunillas (16.2 ± 0.6 Ma, Kay et al., 1994a; 16.2 ± 2.1, Mpodozis et al., 1995), Pastillitos (15.9 ± 0.7 Ma, 16.0 ± 0.9 Ma; Kay et al., 1994a; 16.2 ± 0.7 Ma; 15.9 ± 0.7 Ma, Mpodozis et al., 1995), and Las Cluecas (15.9 ± 1.4 Ma; Kay et al., 1994a) volcanic centers underline the (explosive) magmatic activity within the area of the Ojo de Maricunga complex between ~16 and 15 Ma with some late pyroclastic activity at ~13.8 Ma.

In brief, the zircon ages indicate a continuous magmatic activity at the Ojo de Maricunga volcano over a timespan of ~8.5 Ma, plus late explosive events as indicated by published K-Ar data.

The magmatic evolution of Cerro Maricunga is intimately linked to the flattening of the angle of subduction within the Chilean flat-slab region, at the northern end where the Maricunga belt is situated. The temporal and geochemical evolution within the flat slab and in particular within the metallogenic belt is best shown by Kay and coauthors (Kay et al., 1988, 1991, 1994a, b, 1999, 2014; Kay and Abbruzzi, 1996; Kay and Mpodozis, 2001, 2002).

The temporal evolution of the Maricunga belt during the last ~25 Ma can be demonstrated on the basis of REE patterns (Fig. 16), where the most outstanding feature is the distinct steepening of REE patterns during this period. It is clear that the steepening cannot be strictly correlated with crustal thickness (Kay and Mpodozis, 2002; Kay et al., 2014), however, changes in crustal thickness are clearly indicated. Starting with a crustal thickness of ~45 km in the northern region and ~35–40 km in the southern region of the Maricunga belt the continental crust thickened gradually to > 50 km at ca. 10 Ma and to finally 65–75 km in the southern region before magmatic activity ceased in the total belt (Kay et al., 2014). Currently, the thickness is between 55 and 65 km in the northern and central part of the belt (Heit et al., 2014). The best match between the Cerro Maricunga REE pattern and regional REE patterns representative for the belt is for late Miocene ($La/Yb_{Azufre\ Norte}$ ~31, Kay et al., 1994b; $La/Yb_{Cerro\ Maricunga}$ ~30; Fig. 16). Nonetheless, mineralization took place at Cerro Maricunga in early Miocene at ~17.9 Ma. The late Miocene is described as a period of distinctly thickened crust in the belt, close to the final cessation of magmatic activity. The crust thickening up to ~65–70 km (Goss et al., 2013) in late Miocene is displayed by the steepest REE patterns, clearly deviating from those of Cerro Maricunga, from magmatic centers close to Nevado de Jotabeche (La/Yb ≤ 67, Kay et al., 1994b; La/Yb ≤ 64 in the pre-migration andesites at Dos Hermanos, Goss et al., 2013), representing the latest magmatic stages in the belt. Thus, the REE pattern of early to mid-Miocene rocks at Cerro Maricunga are similar to the REE pattern of late Miocene rocks from the Maricunga belt, which evolved during a phase of distinctly thickened crust. They are distinctly steeper than in coeval rocks from the Maricunga belt from further south, implying a likewise thick crust at the Ojo de Maricunga volcano in mid-Miocene, propably thicker than previously thought.

Reference samples from the El Volcán project, about 50 km south of Cerro Maricunga, show a more diversified REE pattern leading to matches of single samples with Maricunga belt REE patterns for late Oligocene to late Miocene (Fig. 16). The reason for this is the multiple-stage history of Volcán Copiapó hosting the El Volcán project. The mineralization at El Volcán took place at ~11 Ma (Re-Os, –Lohmeier, 2017) and corresponds well to the emplacement time of the gold porphyries of Marte-Lobo, La Pepa and Maricunga Mine.

Notwithstanding the only moderate match of the temporal settings outlined by Kay and coauthors (see above) and the data obtained for Cerro Maricunga, it is undisputed that Cerro Maricunga formed in a phase of advanced crustal evolution in the belt. The magma source region can be located at a depth of ~45 km using the ratio of LREE to HREE, which indicates the transition from a garnet-poor gabbroic residue, equilibrated at ~30–45 km depth, to an anhydrous garnet-bearing granulitic or eclogitic residue, equilibrated at > 45–50 km depth (compare Kay and Mpodozis, 2001). The retention of REEs by amphibole fractionation in the residuum can be excluded for Cerro Maricunga due to a minor depletion in MREE. The assimilation of old lower crust is evident for Cerro Maricunga magmas, and corresponds with investigations of Walker et al. (1991), Trumbull et al. (1999) and Kay et al. (2014). The Cerro Maricunga igneous rocks display both an arc-like mantle signature and a crustal component within their magma source region (Fig. 17), which is best explained by a mixture of mantle-derived melts and melts of lower crust, maybe added by components

entrained before by fore-arc subduction erosion. The geochemical data show that upper crustal signatures are suppressed and deep magma source signatures dominate.

Evaluating the above short outlined temporal and geochemical framework, it is apparent that the thickening of the continental crust in the central part of the Maricunga belt, in the surroundings of Ojo de Maricunga, was more advanced in early and mid-Miocene as previously assumed. This is in accordance with the general situation in the flat-slab segment with crustal thickening in the northern region (~28°S) earlier than in the southern region (~33°S) as shown by Kay et al. (1991), and the increase in crustal thickness from ~35 to 40 km in late Oligocene to ~55–65 km in late Miocene in the north.

The Maricunga belt is a prime example for the transition from porphyry to epithermal gold mineralization (Vila and Sillitoe, 1991; Muntean and Einaudi, 2001). Several attempts were made to characterize and constrain the timeframe of gold mineralization within the belt. The approaches of Kay and Abbruzzi (1996) and Kay et al. (1991, 1999) considered a connection between the temporal and magmatic evolution and displayed a clear timeframe for the formation of the gold porphyries (Fig. 17). The geochemical data of Cerro Maricunga and of the gold porphyries do not match, explicable first by less fractionated REE patterns of the magmatic system of the gold porphyries, and second by a different temporal setting. Whereas the gold porphyries formed at 13 to 11 Ma, mineralization at Cerro Maricunga took place 5 to 7 Ma earlier. Nonetheless, the fundamental prerequisite for mineralization, the release of low-salinity aqueous fluids via breakdown of amphibole in the lower continental crust is fulfilled at Cerro Maricunga. Mineralization at Cerro Maricunga took place within the period 20 to 17 Ma, described as virtual volcanic lull by Mpodozis et al. (1995) and Kay et al. (1999), which is probably a particularly favorable setting for porphyry-epithermal systems.

In short, ore formation at Cerro Maricunga overlaps with the establishment of the flat-slab setting at ~18 Ma, and with documented changes in the magma source region between 18 and 16 Ma (Kay et al., 1988), but does not coincide with the emplacement of the gold porphyries of e.g. Marte-Lobo at 13 to 11 Ma (Kay et al., 1994b). Coeval magmatic activity took place at Pantanillo (18.6 ± 0.8 Ma; Mpodozis, 1995), Domo Torito (18.6 ± 1.3 Ma; Cornejo et al., 1993) and Volcán Jotabeche Norte (18.1 ± 2.0 Ma; Mpodozis, 1995). Magmatic pulses in the neighboring La Coipa domain are slightly younger with 17.3 ± 0.5 Ma (Sillitoe et al., 1991). In general, ages obtained by Re-Os dating are slightly older than those by Ar-Ar dating (Ciobanu et al., 2013), so that a coeval magmatic evolution at Cerro Maricunga and La Coipa is likely.

### 5.5. Cerro Maricunga igneous rocks in the Chilean subduction context

Active continental margins are the major sites for continental magmatism from pristine basaltic rocks to andesites and to more evolved variants like dacites and rhyolites. The Cerro Maricunga igneous rocks have a somewhat uncommon trace-element signature for andesites with Andean-type linkage. Nonetheless, the andesites, rare daciandesites and dacites of this suite are common calc-alkaline rocks of the medium-K series with a clear tendency towards the high-K series. The igneous rocks are related to an uplifted Proterozoic basement that was so far assumed, but for the southern part of the CVZ only indirectly documented by Nd isotopes. During ascent from the lower continental crust the magmas underwent inevitably some changes during AFC processes, including the assimilation of Permian and Triassic country rocks, but they preserved largely the inherited trace-element signature from their source region.

The magmas were probably formed in a MASH-like zone (Hildreth, 1981; Hildreth and Moorbath, 1988) or within a deep crustal “hot zone”, i.e. a site of emplacement of mantle-derived hydrous basalt dikes into the lower crust implying melting of lower crust and the formation of mixed magmas (Annen et al., 2006; Jackson et al., 2018). Inherent trace element and isotope compositions are thus a function of the surrounding metasedimentary and metaigneous basement plus earlier basalt intrusions. Due to high $H_2O$-contents, these melts rise rapidly into shallower crustal levels where crystallization can take place within magma chambers.

The actual mineralization phase took place at ~17.9 Ma related to particularly hydrous magma and the formation of an extensive diatreme system. The aqueous fluids initially originated from the breakdown of amphibole within the magma column and the lower crust, with successive dehydration of the lower crust at a depth of ~45 km, where the magmatic residue passed from amphibolite facies to granulite facies conditions. This transition took place in the area of Cerro Maricunga at ~18 Ma, and about 6–8 Ma later further south when the gold porphyries in the central and southern Maricunga belt formed.

## 6. Conclusions

Gold mineralization at Cerro Maricunga is hosted in an interwoven setting of porphyry intrusions, flows, dikes and diverse breccia types of andesite composition, all forming part of a large diatreme system. In particular, phreatomagmatic and phreatic processes contributed to the formation of the synmineral diatreme complex. The formation of the diatreme provided increased permeability and allowed the set-up of a large hydrothermal system in which porphyry and epithermal mineralization overlap. The evolution of the diatreme complex, involving explosive interaction with groundwater, occurred at for porphyry systems exceptionally shallow levels. The formation of the diatreme complex took place during the adjustment of the flat slab setting in a time of increased crustal thickness. The magmas at Cerro Maricunga show a special adakite-like signature, which was generated during amphibole breakdown and at garnet stability in thickened lower continental crust. The thickening of continental crust might be more advanced in the northern region of the belt in early to mid-Miocene than previously assumed. Proterozoic basement is indicated by Nd model ages and inherited zircon.

## Acknowledgement

The first author had the opportunity to work in this project for Atacama Pacific Gold Corporation in the field season of 2010/2011, and to develop a PhD thesis, from which the main information is extracted, during subsequent research work at Technical University of Clausthal. This work was supported by Atacama Pacific Gold Corporation. It was a pleasure to work in the field with Andrew Hodgkin. Thanks for exciting discussions to Natasha Tschischow and Alonso Cepeda from Atacama Pacific, as well as to (†)Eike Gierth from the Technical University of Clausthal. Thanks to Kurt Mengel for free access to EMPA, to Karl Strauβ for patience and many discussions, and to Ulf Hemmerling for preparation of thin sections (all Technical University of Clausthal). Thanks to Helene Brätz (GeoZentrum Nordbayern, Friedrich-Alexander University Erlangen-Nürnberg) and Harald Strauβ (Institute of Geology and Paleontology, Westfälische Wilhelms University of Münster) for analytical assistance.

## Appendix A. Supplementary data

Supplementary data to this article can be found online at https://doi.org/10.1016/j.jsames.2019.03.003.

## Formatting of funding sources

This study comprises information worked out during the PhD project of the first author. Analytical work was partially funded by Atacama Pacific Gold Corporation.

## References


Alpers, C.N., Brimhall, G.H., 1988. Middle Miocene climatic change in the Atacama Desert, northern Chile: evidence from supergene mineralization at La Escondina. Geol. Soc. Am. Bull. 100, 1640–1656.

Annen, C., Blundy, J.D., Sparks, R.S.J., 2006. The genesis of intermediate and silicic magmas in deep crustal hot zones. J. Petrol. 47, 505–539.

Bineli Betsi, T., Lentz, D.R., 2010. The nature of "quartz eyes" hosted by dykes associated with Au-Bi-As-Cu, Mo-Cu, and base-metal-Au-Ag mineral occurrences in the Mountain Freegold region (Dawson Range), Yukon, Canada. J. Geosci. 55, 347–368.

Bissig, T., Clark, A.H., Lee, J.K.W., von Quadt, A., 2003. Petrogenetic and metallogenetic responses to Miocene slab flattening: new constraints from the El Indio-Pascua Au-Ag-Cu belt, Chile/Argentine. Miner. Deposita 38, 844–862.

Black, L.P., Kamo, S.L., Allen, C.M., Aleinikoff, J.N., Davis, D.W., Korsch, R.J., Foudoulis, C., 2003. Temora 1: a new zircon standard for Phanerozoic U-Pb geochronology. Chem. Geol. 200, 155–170.

Breitkreuz, C., Bahlburg, H., Delakowitz, B., Pichowiak, S., 1989. Palaeozoic volcanic events in the central Andes. J. South Am. Earth Sci. 2, 171–189.

Castillo, P.R., Janney, P.E., Solidum, R.U., 1999. Petrology and geochemistry of Camiguin Island, southern Philippines: insights to the source of adakites and other lavas in a complex arc setting. Contrib. Mineral. Petrol. 134, 33–51.

Ciobanu, C.L., Cook, N.J., Kelson, C.R., Guerin, R., Kalleske, N., Danyusjevsky, L., 2013. Trace element heterogeneity in molybdenite fingerprints stages of mineralization. Chem. Geol. 347, 175–189.

Conca, L., Guzmán, C., Magri, E., 2014. NI 43-101 Technical report on the Cerro Maricunga project, pre-feasibility study Atacama region. Chile 333. http://atacamapacific.com/investors/pdf/cerro-maricunga-technical-report-141006.pdf.

Cornejo, P., Mpodozis, C., Ramírez, C.F., Tomlinson, A., 1993. Estudio geológico de la Región de Potrerillos y El Salvador. Servicio Nacional de Geología y Minería – Corporación del Cobre, vol. 1. pp. 258 Informe registrado IR-93-01.

Davidson, J., Mpodozis, C., 1991. Regional geologic setting of epithermal gold deposits, Chile. Econ. Geol. 86, 1174–1186.

Defant, M.J., Drummond, M.S., 1990. Derivation of some modern arc magmas by melting of young subducted lithosphere. Nature 347, 662–665.

Defant, M.J., Drummond, M.S., 1993. Mount St. Helens: potential example of the partial melting of the subducted lithosphere in a volcanic arc. Geology 21, 547–550.

Defant, M.J., Richerson, P.M., de Boer, J.Z., Stewart, R.H., Maury, R.C., Bellon, H., Drummond, M.S., Feigenson, M.D., Jackson, T.E., 1991. Dacite genesis via both slab melting and differentiation: petrogenesis of La Yeguada volcanic complex, Panama. J. Petrol. 32, 1101–1142.

Evenstar, L., Hartley, A., Rice, C., Stuart, F., Mather, A., Chong, G., 2005. Miocene-Pliocene climate change in the Peru-Chile desert. In: Extended Abstracts, 6th International Symposium on Andean Geodynamics, pp. 258–260.

Field, C.W., Fifarek, R.H., 1985. Light stable-isotope systematics in the epithermal environment. Rev. Econ. Geol. 2, 99–128.

Ghiorso, M.S., Gualda, G.A.R., 2013. A method for estimating the activity of titania in magmatic liquids from the compositions of coexisting rhombohedral and cubic iron-titanium oxides. Contrib. Mineral. Petrol. 165, 73–81.

González-Ferrán, O., Baker, P.E., Rex, D.C., 1985. Tectonic-volcanic discontinuity at latitude 27° south Andean range, associated with Nazca plate subduction. Tectonophysics 112, 423–441.

Goss, A.R., Kay, S.M., 2009. Extreme high field strength element (HFSE) depletion and near-chondritic Nb/Ta ratios in Central Andean adakite-like lavas (~27°S, ~68°W). Earth Planet. Sci. Lett. 279, 97–109.

Goss, A.R., Kay, S.M., Mpodozis, C., 2013. Andean adakite-like high-Mg andesites on the northern margin of the Chilean-Pampean flat-slab (27-28.5°S) associated with frontal arc migration and fore-arc subduction erosion. J. Petrol. 54, 2193–2234.

Gustafson, L.B., Hunt, J.P., 1975. The porphyry copper deposit at El Salvador, Chile. Econ. Geol. 70, 857–912.

Harris, A.C., Kamenetsky, V.S., White, N.C., 2003. The magmatic-hydrothermal transition: volatile separation in silicic rocks at Bajo de la Alumbrera porphyry Cu-Au deposit, NW Argentina. In: Blevin, P., Champion, D. (Eds.), The Ishihara Symposium: Granites and Associated Metallogenesis. GEMOC Macquarie University, Sydney, Australia, pp. 69–74.

Harris, A.C., Kamenetsky, V.S., White, N.C., Steele, D.A., 2004. Volatile phase separation in silicic magmas at Bajo de la Alumbrera porphyry Cu-Au deposit, NW Argentina. Resour. Geol. 54, 341–356.

Hayden, L.A., Watson, E.B., 2007. Rutile saturation in hydrous siliceous melts and its bearing on Ti-thermometry of quartz and zircon. Earth Planet. Sci. Lett. 258, 561–568.

Heit, B., Bianchi, M., Yuan, X., Kay, S.M., Sandvol, E., Kumar, P., Kind, R., Alonso, R.N., Brown, L.D., Comte, D., 2014. Structure of the crust and the lithosphere beneath the southern Puna plateau from teleseismic receiver functions. Earth Planet. Sci. Lett. 385, 1–11.

Hildreth, W., 1981. Gradients in silicic magma chambers: implications for lithospheric magmatism. J. Geophys. Res. 86 B11 10153-10129.

Hildreth, W., Moorbath, S., 1988. Crustal contributions to arc magmatism in the Andes of Central Chile. Contrib. Mineral. Petrol. 98, 455–489.

Hollings, P., Cooke, D., Clark, A., 2005. Regional geochemistry of Tertiary igneous rocks in central Chile: implications for the geodynamic environment of giant porphyry copper and epithermal gold mineralization. Econ. Geol. 100, 887–904.

Homepage Kinross, February 2019a. La Coipa. http://fb.kinross.com/operations/operation-la-coipa-chile.aspx.

Homepage Kinross, February 2019b. Aldebarán. http://fb.kinross.com/operations/dp-cerro-casale-chile.aspx.

Homepage Kingsgate, February 2019. Nueva Esperanza. https://www.kingsgate.com.au/nueva-esperanza-overview/.

Hopwood, T.P., 1976. "Quartz-eye"-bearing porphyroidal rocks and volcanogenic massive sulfide deposits. Econ. Geol. 71, 589–612.

Jackson, M.D., Blundy, J., Sparks, R.S.J., 2018. Chemical differentiation, cold storage and remobilization of magma in the Earth's crust. Nature 564, 405–409.

Jannas, R.R., Beane, R.E., Ahler, B.A., Brosnahan, D.R., 1990. Gold and copper mineralization at the El Indio deposit, Chile. J. Geochem. Explor. 36, 233–266.

Kay, R.W., 1978. Aleutian magnesian andesites: melts from subducted Pacific ocean crust. J. Volcanol. Geotherm. Res. 4, 117–132.

Kay, R.W., Kay, S.M., 2002. Andean adakites: three ways to make them. Acta Petrol. Sin. 18, 303–311.

Kay, S.M., Abbruzzi, J.M., 1996. Magmatic evidence for Neogene lithospheric evolution of the central Andean "flat-slab" between 30°S and 32°S. Tectonophysics 259, 15–28.

Kay, S.M., Maksaev, V., Moscoso, R., Mpodozis, C., Nasi, C., 1987. Probing the evolving Andean lithosphere: mid-late Tertiary magmatism in Chile (29°-30°30'S) over the modern zone of subhorizontal subduction. J. Geophys. Res. 92 B7, 6173–6189.

Kay, S.M., Maksaev, V., Moscoso, R., Mpodozis, C., Nasi, C., Gordillo, C.E., 1988. Tertiary Andean magmatism in Chile and Argentina between 28°S and 33°S: correlation of magmatic chemistry with a changing Benioff zone. J. South Am. Earth Sci. 1, 21–38.

Kay, S.M., Mpodozis, C., 2001. Central Andean ore deposits linked to evolving shallow subduction systems and thickening crust. GSA Today (Geol. Soc. Am.) 11, 4–9.

Kay, S.M., Mpodozis, C., 2002. Magmatism as a probe to the Neogene shallowing of the Nazca plate beneath the modern Chilean flat-slab. J. South Am. Earth Sci. 15, 39–57.

Kay, S.M., Mpodozis, C., Coira, B., 1996. Central Andean mantle-derived basalts and Neogene mantle enrichment beneath the Puna plateau. In: Colloques et séminaires ORSTOM, Troisième symposium international sur la Géodynamique andine. Saint-Malo, France, pp. 583–586.

Kay, S.M., Mpodozis, C., Coira, B., 1999. Neogene Magmatism, Tectonism, and Mineral Deposits of the Central Andes (22° to 33°S Latitude), vol. 7. Society of Economic Geologists Special Publications, pp. 27–59.

Kay, S.M., Mpodozis, C., Cornejo, P., 1994a. Late Cenozoic evolution of the southern CVZ (26-28°S): a case of progressive crustal thickening and lithospheric thinning. In: Actas, VII Congreso Geológico Chileno, Concepción, pp. 1372–1377.

Kay, S.M., Mpodozis, C., Gardeweg, M., 2014. Magma source and tectonic setting of Central Andean andesites (25.5 – 28°S) related to crustal thickening, forearc subduction erosion and delamination. Geological Society of London, Special Publications 385, 303–334.

Kay, S.M., Mpodozis, C., Ramos, V.A., Munizaga, F., 1991. Magma source variations for mid-late Tertiary magmatic rocks associated with a shallowing subduction zone and a thickening crust in the central Andes (28 to 33°S). Geol. Soc. Am. Spec. Pap. 265, 113–137.

Kay, S.M., Mpodozis, C., Tittler, A., Cornejo, P., 1994b. Tertiary magmatic evolution of the Maricunga mineral belt in Chile. Int. Geol. Rev. 36, 1079–1112.

Lange, R.A., Frey, H.M., Hector, J., 2009. A thermodynamic model for the plagioclase-liquid hygrometer/thermometer. Am. Mineral. 94, 494–506.

Le Maitre, R.W., Bateman, P., Dudek, A., Keller, J., Lameyre, J., Le Bas, M.J., Sabine, P.A., Schmid, R., Sorensen, H., Streckeisen, A., Woolley, A.R., Zanettin, B., 1989. A Classification of Igneous Rocks and Glossary of Terms: Recommendations of the International Union of Geological Sciences Subcommission on the Systematics of Igneous Rocks. Blackwell Scientific Publications, Oxford, pp. 193.

Lohmeier, S., 2017. The Cerro Maricunga Gold Deposit, Maricunga Belt, Northern Chile: Magmatic Evolution and Au Mineralization. Dissertation. Technical University of Clausthal, pp. 283.

Lohmeier, S., Lehmann, B., Schneider, A., 2013. Geological and geochemical features of the Cerro Maricunga project in the Maricunga gold belt, northern Chile. In: Extended Abstracts, 12th Biennial Meeting SGA, Uppsala, Sweden, pp. 825–828.

Lohmeier, S., Schneider, A., Lehmann, B., unpublished results, a. Veinlet Petrography and Gold Mineralization of the Cerro Maricunga Gold Deposit, Maricunga Belt, Northern Chile.

Lorenz, V., 2003. Maar-diatreme volcanoes, their formation, and their setting in hard-rock or soft-rock environments. Geolines 15, 72–83.

Ludwig, K.R., 2005a. SQUID 1.12 a User's Manual. A Geochronological Toolkit for Microsoft Excel. Berkeley Geochronology Center Special Publication, pp. 1–22.

Ludwig, K.R., 2005b. User's Manual for ISOPLOT/Ex 3.22. A Geochronological Toolkit for Microsoft Excel. Berkeley Geochronology Center Special Publication, pp. 1–71.

Lyubetskaya, T., Korenaga, J., 2007. Chemical composition of Earth's primitive mantle and its variance: 1. Method and results. J. Geophys. Res. 112, B03211.

Maksaev, J.V., Moscoso, D.R., Mpodozis, M.C., Nasi, P.C., 1984. Las unidades volcánicas y plutónicas del Cenozoico superior en la alta cordillera del Norte Chico (29°-31°S): geología, alteración hidrotermal y mineralización. Rev. Geol. Chile 21, 11–51.

Mamani, M., Tassara, A., Wörner, G., 2008. Compositional and structural control of crustal domains in the central Andes. Geochem. Geophys. Geosyst. 9, 1–13.

McKee, E.H., Robinson, A.C., Rybuta, J.J., Cuitiño, L., Moscoso, R.D., 1994. Age and Sr isotopic composition of volcanic rocks in the Maricunga belt, Chile: implications for magma sources. J. South Am. Earth Sci. 7, 167–177.

Mpodozis, C., 1995. Evolución magmática terciaria de la región de transición entre la CVZ y la zona de subducción subhorizontal de los Andes chilenos. Servicio Nacional de Geología y Minería informe final proyecto Fondecyl 149/92.

Mpodozis, C., Cornejo, P., Gardeweg, M., Kay, S.M., 1994. El complejo volcánico Copiapó, Mioceno superior, Franja de Maricunga (27°30'S). In: Proceedings, 7th Chilean Geological Congress. Concepción, Chile, pp. 1125–1129.

Mpodozis, C., Cornejo, P., Kay, S.M., Tittler, A., 1995. La Franja de Maricunga: síntesis de la evolución del frente volcánico Oligoceno-Mioceno de la zona sur de los Andes centrales. Rev. Geol. Chile 21, 273–313.

Muntean, J.L., Einaudi, M.T., 2001. Porphyry-epithermal transition: Maricunga belt,

northern Chile. Econ. Geol. 96, 743–772.
Ohmoto, H., Rye, R.O., 1979. Isotopes of sulfur and carbon. In: Barnes, H.L. (Ed.), Geochemistry of Hydrothermal Ore Deposits, second ed. Wiley Interscience, New York, pp. 509–567.
Oviedo, L., Fuster, N., Tschischow, N., Ribba, L., Zuccone, A., Grez, E., Aguilar, A., 1991. General geology of La Coipa precious metal deposit, Atacama, Chile. Econ. Geol. 86, 1287–1300.
Pearce, J.A., 1983. Role of the subcontinental lithosphere in magma genesis at active continental margins. In: Hawksworth, M.J., Nurry, M.L. (Eds.), Continental Basalts and Mantle Xenoliths. Shiva, Nantwich, pp. 230–249.
Pearce, J.A., Parkinson, I.J., 1993. Trace element models for mantle melting: application to volcanic arc petrogenesis. 76. Geological Society Special Publications, pp. 373–403.
Piccoli, P.M., Candela, P.A., 2002. Apatite in igneous systems. Rev. Mineral. Geochem. 48, 255–292.
Prouteau, G., Scaillet, B., Pichavant, M., Maury, R., 2001. Evidence for mantle metasomatism by hydrous silicic melts derived from subducted oceanic crust. Nature 410, 197–200.
Putirka, K.D., 2005. Igneous thermometers and barometers based on plagioclase + liquid equilibria: tests of some existing models and new calibrations. Am. Mineral. 90, 336–346.
Putirka, K.D., 2008. Thermometers and barometers for volcanic systems. Rev. Mineral. Geochem. 69, 61–120.
Quirt, G.S., 1972. A Potassium-Argon Geochronological Investigation of the Andean Mobile Belt of North Central Chile. PhD thesis. Queen's University, pp. 234.
Ramos, V.A., Vujovich, G., Martino, R., Otamendi, J., 2010. Pampia: a large cratonic block missing in the Rodinia supercontinent. J. Geodyn. 50, 243–255.
Richard, P., Shimizu, N., Allègre, C.J., 1976. $^{143}Nd/^{144}Nd$, a natural tracer: an application to oceanic basalts. Earth Planet. Sci. Lett. 31, 269–278.
Richards, J.P., 2009. Postsubduction porphyry Cu-Au and epithermal Au deposits: products of remelting of subduction-modified lithosphere. Geology 37, 247–250.
Richards, J.P., 2011. High Sr/Y arc magmas and porphyry Cu ± Mo ± Au deposits: just add water. Econ. Geol. 106, 1075–1081.
Richards, J.P., Kerrich, R., 2007. Special paper: adakite-like rocks: their diverse origins and questionable role in metallogenesis. Econ. Geol. 102, 537–576.
Richards, J.P., Spell, T., Rameh, E., Razique, A., Fletcher, T., 2012. High Sr/Y magmas reflect arc maturity, high magmatic water content, and porphyry Cu ± Mo ± Au potential: examples from the Tethyan arcs of central and eastern Iran and western Pakistan. Econ. Geol. 107, 295–332.
Rickwood, P.C., 1989. Boundary lines within petrologic diagrams which use oxides of major and minor elements. Lithos 22, 247–263.
Rollinson, H., 1993. Using Geochemical Data: Evaluation, Presentation, Interpretation. Taylor and Francis, London, pp. 353.
Saunders, A.D., Tarney, J., 1984. Geochemical characteristic of basaltic volcanism within back-arc basins. Geol. Soc. Spec. Publ. 16, 59–76.
Schulz, F., 1997. Geologie und Geochemie der copper porphyry-Lagerstätte Los Pelambres/Chile. Diplom thesis. Technical University of Clausthal.
Seal II., R.R., 2006. Sulfur isotope geochemistry of sulfide minerals. Rev. Mineral. Geochem. 61, 633–677.
Seal II., R.R., Alpers, C.N., Rye, R.O., 2000. Stable isotope systematics of sulfate minerals. Rev. Mineral. Geochem. 40, 541–602.
Sheppard, S.M.F., 1977. The Cornubian batholith, SW England: D/H and $^{18}O/^{16}O$ studies of kaolinite and other alteration minerals. Journal of the Geological Society of London 133, 573–591.
Sillitoe, R.H., 1985. Ore-related breccias in volcanoplutonic arcs. Econ. Geol. 80, 1467–1514.
Sillitoe, R.H., 2000. Gold-rich porphyry deposits: descriptive and genetic models and their role in exploration and discovery. Rev. Econ. Geol. 13, 315–345.
Sillitoe, R.H., 2010. Porphyry copper systems. Econ. Geol. 105, 3–41.
Sillitoe, R.H., McKee, E.H., 1996. Age of supergene oxidation and enrichment in the Chilean porphyry copper province. Econ. Geol. 91, 164–179.
Sillitoe, R.H., McKee, E.H., Vila, T., 1991. Reconnaissance K-Ar geochronology of the Maricunga gold-silver belt, northern Chile. Econ. Geol. 86, 1261–1270.
Sillitoe, R.H., Tolman, J., van Kerkvoort, G., 2013. Geology of the Caspiche porphyry gold-copper deposit, Maricunga belt, northern Chile. Econ. Geol. 108, 585–604.
Stacey, J.S., Kramers, J.D., 1975. Approximation of terrestrial lead isotope evolution by a two-stage model. Earth Planet. Sci. Lett. 26, 207–221.
Steiger, R.H., Jäger, E., 1977. Submission on geochronology: convention on the use of decay constants in geo- and cosmochronology. Earth Planet. Sci. Lett. 36, 359–362.
Stern, C.R., Kilian, R., 1996. Role of the subducted slab, mantle wedge and continental crust in the generation of adakites from the Andean Austral Volcanic Zone. Contrib. Mineral. Petrol. 123, 263–281.
Streck, M.J., 2008. Mineral textures and zoning as evidence for open system processes. Rev. Mineral. Geochem. 69, 595–622.
Sun, S.-S., McDonough, W.F., 1989. Chemical and isotopic systematics of oceanic basalts: implications for mantle composition and processes. Geol. Soc. Spec. Publ. 42, 313–345.
Taylor, H.P., 1974. The application of oxygen and hydrogen isotope studies to problems of hydrothermal alteration and ore deposition. Econ. Geol. 69, 843–883.
Taylor, R., 2009. Ore Textures: Recognition and Interpretation. Springer, Dordrecht, pp. 288.
Taylor, S.R., McLennan, S.M., 1985. The Continental Crust: its Composition and Evolution. Blackwell Scientific Publications, Carlton, pp. 312.
Tittler, A., 1995. The Chemistry of Miocene Andean Volcanic Rocks from the "Flat-slab" to Central Volcanic Zone Transition, Chile, 26° to 28°S. M.S. thesis. Cornell University, pp. 144.
Thomas, J.B., Watson, E.B., 2012. Application of the Ti-in-quartz thermobarometer to rutile-free systems. Reply to: a comment on: 'TitaniQ under pressure: the effect of pressure and temperature on the solubility of Ti in quartz' by Thomas et al. Contrib. Mineral. Petrol. 164, 369–374.
Thomas, J.B., Watson, E.B., Spear, F.S., Shemella, P.T., Nayak, S.K., Lanzirotti, A., 2010. TitaniQ under pressure: the effect of pressure and temperature on the solubility of Ti in quartz. Contrib. Mineral. Petrol. 160, 743–759.
Trumbull, R.B., Wittenbrink, R., Hahne, K., Emmermann, R., Büsch, W., Gerstenberger, H., Siebel, W., 1999. Evidence for late Miocene to Recent contamination of arc andesites by crystal melts in the Chilean Andes (25-26°S) and its geodynamic implications. J. South Am. Earth Sci. 12, 135–155.
Ulmer, P., 2001. Partial melting in the mantle wedge - the role of $H_2O$ in the genesis of mantle-derived 'arc-related' magmas. Phys. Earth Planet. In. 127, 215–232.
Vasyukova, O.V., Gömann, K., Macrae, C.M., Kamenetsky, V.S., 2010. Origin of quartz-eyes from porphyry-type deposits. In: Conference Abstracts, 20th Goldschmidt Conference, Knoxville, USA, pp. A1076.
Vernon, R.H., 1986. Evaluation of the "quartz-eye" hypothesis. Econ. Geol. 81, 1520–1527.
Vernon, R.H., 1987. Evaluation of the "quartz-eye" hypothesis - a Reply. Econ. Geol. 82, 1083–1084.
Vila, T., Sillitoe, R.H., 1991. Gold-rich porphyry systems in the Maricunga belt, northern Chile. Econ. Geol. 86, 1238–1260.
Vila, T., Sillitoe, R.H., Betzhold, J., Viteri, E., 1991. The porphyry gold deposit at Marte, northern Chile. Econ. Geol. 86, 1271–1286.
Walker, J.A., Moulds, T.N., Zentilli, M., Feigenson, M.D., 1991. Spatial and temporal variations in volcanics of the andean central volcanic zone (26 to 28°S). Geol. Soc. Am. Spec. Pap. 265, 139–155.
Wark, D.A., Watson, E.B., 2006. TitaniQ: a titanium-in-quartz geothermometer. Contrib. Mineral. Petrol. 152, 743–754.
Watt, G.R., Wright, P., Galloway, S., McLean, C., 1997. Cathodoluminescence and trace element zoning in quartz phenocrysts and xenocrysts. Geochem. Cosmochim. Acta 61, 4337–4348.
Wiedenbeck, M., Allé, P., Corfu, F., Griffin, W.L., Meier, M., Oberli, F., von Quadt, A., Roddick, J.C., Spiegel, W., 1995. Three natural zircon standards for U-Th-Pb, Lu-Hf, trace element and REE analyses. Geostand. Newsl. 19, 1–23.
Williams, P., Carmichael, A., 1987. Evaluation of the "quartz-eye" hypothesis – a discussion. Econ. Geol. 82, 1081–1082.
Zentilli, M., 1974. Geological Evolution and Metallogenetic Relationships in the Andes of Northern Chile between 26° and 29°S. PhD thesis. Queen's University 460 pp.